

PAPER • OPEN ACCESS

PROTO-SPHERA: a magnetic confinement experiment which emulates the jet + torus astrophysical plasmas
















To cite this article: Franco Alladio *et al* 2024 *Plasma Phys. Control. Fusion* **66** 035011

View the [article online](#) for updates and enhancements.

You may also like

- [A new indirect measurement method of the electron temperature for the Proto-sphera's pinch plasma](#)
D. Iannarelli, F. Napoli, F. Alladio et al.
- [Ideal MHD stability limits of the PROTO-SPHERA configuration](#)
P. Micozzi, F. Alladio, A. Mancuso et al.
- [Final results of the first phase of the PROTO-SPHERA experiment: obtainment of the full current stable screw pinch and first evidences of the jet + torus combined plasma configuration](#)
Paolo MICOZZI, Franco ALLADIO, Alessandro MANCUSO et al.

PROTO-SPHERA: a magnetic confinement experiment which emulates the jet + torus astrophysical plasmas

Franco Alladio^{1,*} , Paolo Micozzi^{1,2} , Luca Boncagni² , Annamaria Pau³ , Shayesteh Naghinajad⁴ , Samanta Macera^{5,9} , Yacopo Damizia⁶ , Paolo Buratti^{1,2,7} , Francesco Filippi² , Giuseppe Galatola Teka² , Francesco Giammanco^{8,10} , Edmondo Giovannozzi² , Matteo Iafrazi² , Alessandro Lampasi²  and Paolo Marsili⁸ 

¹ INAF—IAPS, Via Fosso del Cavaliere 100, 0133, Rome, Italy

² NUC Dipartimento Nucleare, ENEA Agenzia Nazionale per Le Nuove Tecnologie l'Energia e lo Sviluppo Economico Sostenibile, CR Frascati CP 65 Via E Fermi 45, Frascati (Rome), 00044, Italy

³ Department of Structural and Geotechnical Engineering, Sapienza University of Rome, Via Eudossiana 18, Roma, 00184, Italy

⁴ Sapienza University of Rome, Department of Astronautical, Electrical and Energy Engineering, Via Eudossiana 18, Roma, 00184, Italy

⁵ GSSI, Viale Francesco Crispi 7, 67100 L'Aquila, Italy

⁶ Department of Electrical Engineering and Electronics, University of Liverpool, Liverpool L69 3GJ, United Kingdom

⁷ Dipartimento di Ing. Civile ed Informatica, Università di Roma 'Tor Vergata', 00133 Rome, Italy

⁸ Physics Department, University of Pisa, Faculty of Natural Sciences Mathematics and Physics, Largo B. Pontecorvo 3, 56127 Pisa, Italy

⁹ Laboratori Nazionali del Gran Sasso, INFN, Via G. Acitelli 22, Assergi (L'Aquila), 67100, Italy

E-mail: franco.alladio@protosphaera.it

Received 28 September 2023, revised 16 December 2023

Accepted for publication 22 January 2024

Published 6 February 2024



CrossMark

Abstract

The PROTO-SPHERA experiment, built at the CR-ENEA laboratory in Frascati, was in part inspired by the jet + torus astrophysical plasmas, a rather common morphology in Astrophysics. This paper illustrates how the said plasma morphology can be reproduced in a laboratory with the setup of the PROTO-SPHERA experiment. The experiment as such displayed the appearance and sustainment of a plasma torus around an internal magnetized plasma centerpost (jet) by self-organisation; an entirely unexplored phenomenon to date. The remarkable ideal MHD stability of the PROTO-SPHERA plasma is extremely significant, as it is obtained in a simply connected geometry, inside a perfectly insulating vacuum vessel, and without the need of a nearby stabilizing conducting shell. The concluding sections of this paper deal with application of force-free fields to the Pulsar Wind Nebulae morphology and present an extension of the well-known split-dipole model. Such an extension provides a natural description of the presence of tori around the Pulsar plasma jets. In addition, similarities and differences between the laboratory and the astrophysical jet + torus plasmas are detailed.

Keywords: magnetic confinement, pulsar wind nebulae, force-free fields, magnetic reconnection, ideal MHD stability, 3D tomography, tokamak, plasma self-organisation

¹⁰ Retired.

* Author to whom any correspondence should be addressed.



1. Introduction

The PROTO-SPHERA experiment [1, 2] was built at the CR-ENEA laboratory in Frascati in an attempt to emulate in the laboratory the jet + torus astrophysical plasmas. This paper tries to compare selected results obtained in the laboratory with observations in Astrophysics. Particular emphasis will be given to the Pulsar Wind Nebula (PWN) objects, which, among the jet + torus astrophysical objects, are the nearest to Earth and those whose observations are the most detailed ones. The first difference between PROTO-SPHERA and its cosmical counterparts, is that in Astrophysics the virial theorem is fulfilled by the gravitational force, whereas in the case of a laboratory experiment it is fulfilled by the magnetic fields produced by poloidal field coils surrounding the plasma. The second difference is that in the astrophysical models the electrical current density \vec{j} in the plasma jet has opposite directions in the 2 hemispheres, whereas in PROTO-SPHERA the plasma current of the jet goes through the center of the magnetic configuration without changing direction. The third difference is that in non-relativistic Astrophysics the solenoidal condition for the plasma current density $\vec{\nabla} \cdot \vec{j} = 0$ is satisfied. On the contrary, in a laboratory experiment the plasma electrostatically charges all nearby metallic conductors present inside the vacuum vessel, but the internal charged metal surfaces cause an $\vec{E} \wedge \vec{B}$ rotation of the overall plasma around its symmetry axis. Recent observation of the tilted azimuthal rotation of the plasma and of the non-axisymmetric nature of the recurring magnetic reconnections, which have a correspondence with the recurring flares of the PWN [3], show that in PROTO-SPHERA the production of closed toroidal flux surfaces is associated with a plasma that acts as a slightly oblique rotator, which is an unexpected similarity to the oblique plasma rotators present in Astrophysics. Notwithstanding the many similarities, remarkable differences exist between the laboratory experiment and the model for PWN, in particular the number of tori around the jets that are present in the two cases (one in the laboratory experiment, two in the astrophysical model) and the localization of magnetic reconnections that occur near such tori.

The paper is organized as follow. Section 2 introduces the jet + torus plasma objects and connects them to the wide subject of magnetic reconnections. Section 3 first sketches the two main plasma physics concepts upon which the PROTO-SPHERA experiment is based: force-free magnetic fields and magnetic helicity, which are linked by magnetic reconnections. Such concepts are detailed in the four Appendices that follow the main paper. Section 3 then expands upon the main features of the physical design of the experiment, comparing it with tokamaks and spheromaks, and details its magnetic structure. The construction and the commissioning of the experiment, up to the present day, are sketched in section 4. The presence of a confined plasma torus in the PROTO-SPHERA experiment is illustrated in section 5, which uses the results of the 3D tomography of the plasma, obtained from its visible light emission. Both formation and sustainment of such a torus can be attributed, as expected from the physical design,

to magnetic reconnections. The main novelty of PROTO-SPHERA is the remarkable ideal MHD stability obtained in the experimental plasmas. Section 6 introduces the up/down odd-symmetric Chandrasekhar–Kendall–Furth (CKF) force-free fields as a model for the plasma of PWN, compares such a model with some astronomical observations and tries to apply it to the unsettled question of magnetic reconnection and of particle acceleration in PWN. Section 7 draws conclusions about the similarities and the differences between what has been obtained in the laboratory and what is observed in the sky. The theory upon which the PROTO-SPHERA experiment is based is reviewed in four Appendices. Appendix A deals with the force-free plasma configurations and with the concept of magnetic helicity for configurations with closed field lines. Appendix B specializes in the homogeneous (or linear, or relaxed) force-free magnetic fields and introduces the up/down even-symmetric unlocalized CKF configurations with closed field lines, as a superposition of simpler well-known force-free fields and illustrates their ideal MHD stability properties. Appendix C extends the equilibrium and the ideal MHD stability analysis to un-relaxed CKF magnetic confinement schemes, which are CKF configurations localized and confined by poloidal magnetic field coils (PF) and filled with high plasma pressure, up to beta values (ratio between the kinetic plasma pressure and the magnetic field pressure) much higher than other plasma confinement systems. Appendix D extends the concept of magnetic helicity to configurations with open field lines terminating on electrodes.

2. Jet + torus plasmas in astrophysics and in the laboratory

Combined plasma configurations, composed by jets and tori are present in PWN, see figures 1(a) and (b), and can be produced in a laboratory: the PROTO-SPHERA experiment [1] has an internal plasma jet -the magnetized centerpost plasma (CP) on the axis of symmetry of the configuration- surrounded by a magnetized spherical torus plasma (ST) orthogonal to the centerpost, see figure 1(c). PROTO-SPHERA was built at the CR-ENEA laboratory in Frascati as an innovative configuration of plasma magnetic confinement, in view of controlled fusion research, and it is quite different from the confinement experiments studied so far. The confined plasma geometry is simply connected: no metal conductor is topologically linked to the plasma torus and the vacuum chamber is a simple cylinder. The vertical CP carries a total plasma current I_{CP} and is sustained by a DC voltage V_e , applied between electrodes placed inside the vacuum vessel; a confined ST carries a total toroidal plasma current I_{ST} and is formed by self-organization around the CP: the lines of force that wind around the centerpost get broken and reconnected into lines of force winding along the torus [2]. The self-organization phenomenon is based on magnetic reconnections [4], which are associated with non-ideal MHD plasma dissipative effects (such as finite resistivity) and are ubiquitous in astrophysical plasmas, from the terrestrial magnetosphere, to the solar corona, to the PWN

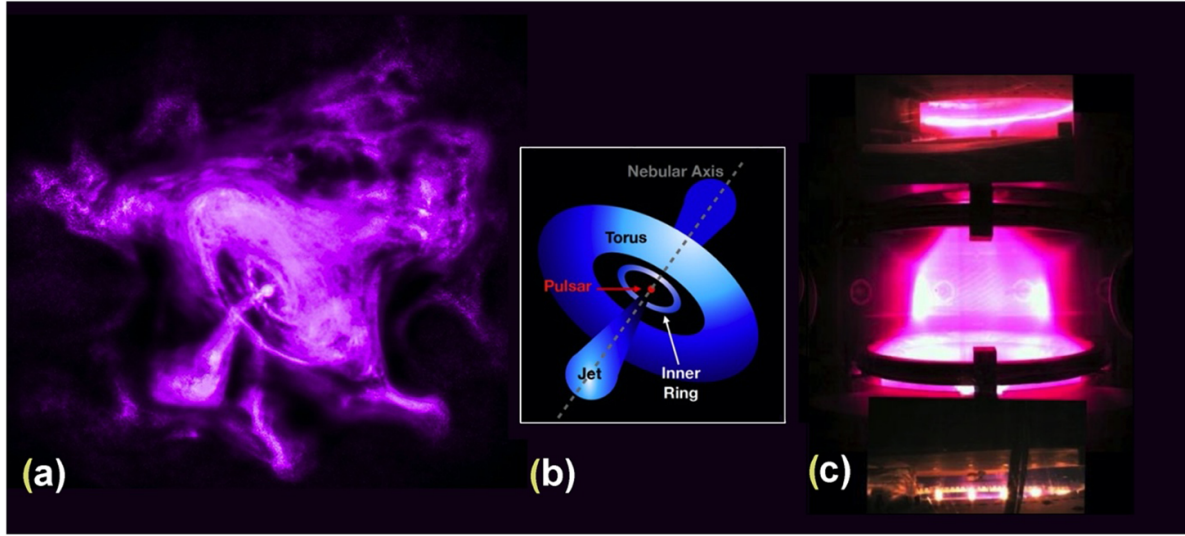


Figure 1. (a) X-ray Chandra image of the Crab PWN, ESA/Hubble credit [5]. (b) Sketch of the observations shown in (a). (c) Visible light image of hydrogen plasma of PROTO-SPHERA, where the vertical centerpost plasma, carrying a total plasma current I_{CP} , is surrounded by a plasma torus, carrying a total toroidal plasma current I_{ST} . The plasma is unique, but this image is composed by 3 independent images: the anodic centerpost plasma (top), impinging on a continuous annular gas-puffed anode; the equatorial centerpost + torus plasma (middle); the cathodic centerpost plasma (bottom), emitted by 54 hot tungsten filaments. Reproduced from [5]. CC BY 4.0. Credit: CXC.

[5] of figure 1(a), and finally to the active galactic nuclei jets, in order of increasing size. The phenomenon of magnetic reconnection can be summarized as follows: near a point, or a curve, where two magnetic field lines nearly touch each other, but have opposite field direction (the so-called X-points), a ‘tearing’ of those lines occurs, followed by a different ‘stitching’ between them. The magnetic field configuration resulting from the reconnection has a lower energy, which leads to thermal plasma heating as well as to super-thermal particles acceleration. In magnetic reconnections, magnetic flux and electric current are transferred as well between magnetic field regions that in an ideal MHD framework would remain disconnected.

3. PROTO-SPHERA, ideas and physical design

While in Astrophysics the appearance of jet + torus is a spontaneous phenomenon lasting for an enormous continuum of time, in the case of the PROTO-SPHERA experiment the appearance and the sustainment of a plasma torus around a central plasma jet was an unexplored phenomenon, and therefore a gamble placed on the self-organisation properties of a plasma. Such an endeavour has at its base two plasma physics concepts that have had, for more than 60 years, and still have quite a relevance in magnetic confinement research. These are the force-free magnetic fields and magnetic helicity injection, which are linked by magnetic reconnections. The theoretical foundations of the two concepts are sketched in the Appendices to this paper, and focus on the aspects relevant to the physical design of the experiment as well as to the interpretation of its results.

Appendix A reviews the force-free magnetic field configurations (dubbed in this paper as *ffmf*), which obey the Beltrami field equation $\vec{\nabla} \wedge \vec{B} = \mu \vec{B}$ [6], which means that the plasma

electric current density \vec{j} is perfectly aligned along the field lines \vec{B} . The relaxation of a magnetized plasma consists in minimizing its magnetic energy with appropriate constraints; the constraint is the conservation of a volume integrated quantity: magnetic helicity $K = \int \vec{A} \cdot \vec{B} dV$ (where \vec{A} is the vector magnetic potential), well-defined for every closed flux tube in a perfectly conducting plasma. Real plasmas are never perfectly conducting, so magnetic reconnections redistribute the magnetic helicity without destroying it [7] and *ffmf*s are the final result of plasma relaxation [8]; this is the reason why the parameter $\mu = \mu_0 \vec{j} \cdot \vec{B} / B^2$ of the Beltrami field is called relaxation parameter. If the relaxation parameter μ is not constant all over the plasma, the magnetic helicity flows from higher to lower μ values: this transfer takes the name of magnetic helicity injection.

Appendix B illustrates the linear *ffmf*s, which have a relaxation parameter $\mu = \mu_0 \vec{j} \cdot \vec{B} / B^2$ constant all over the plasma. Jet + torus configurations exhibiting up/down even-symmetry can be obtained by superimposing the well-known Chandrasekhar–Kendall linear *ffmf* [9] -which describes tori- and the Furth square-toroid *ffmf* [10] -which represents jets; the resulting CKF *ffmf*s are the simplest possible analytical examples of the PROTO-SPHERA jet + torus magnetic configuration (see figure B1). However CKF *ffmf*s have no pressure gradient, $\vec{\nabla} p = 0$, and are unable to confine plasmas of interest for fusion. Moreover, they are unlocalized plasma objects extending over the whole 3D space. Appendix C details the numerical evaluation of un-relaxed ($\vec{j} \wedge \vec{B} \neq 0$, $\vec{\nabla} p \neq 0$) CKF equilibria [11]: they are localized configurations that can be confined by external PF coils and that can be filled up with plasma pressure (see figure C1), while remaining ideally stable up to the remarkable value of volume-averaged beta values $\langle \beta \rangle_{vol} = 1$ (see figure C2). For un-relaxed CKF

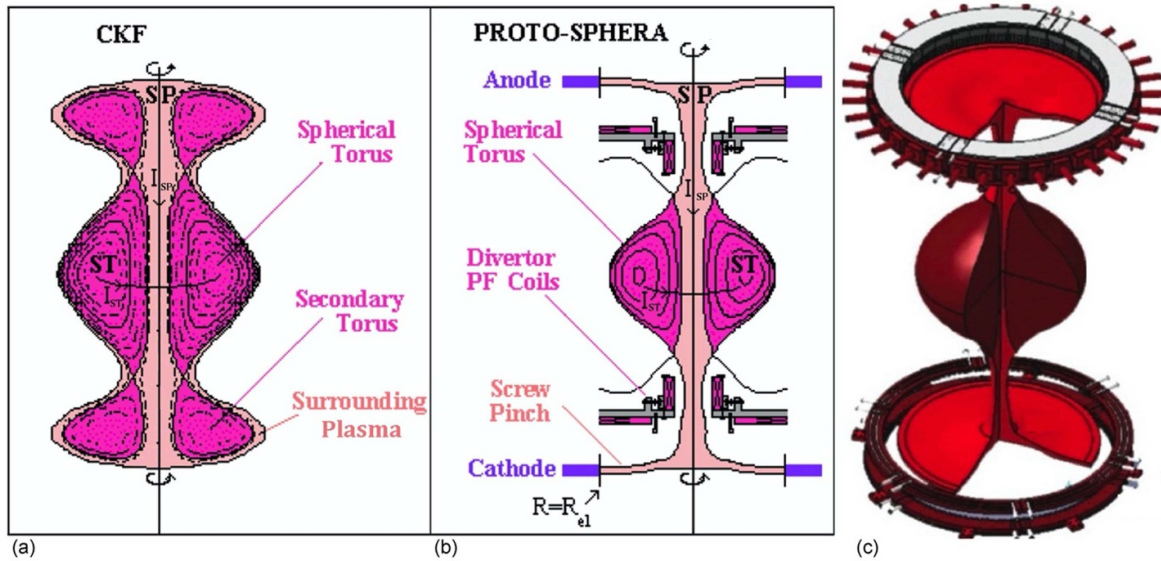


Figure 2. The comparison between (a) an un-relaxed CKF configuration -enclosed by a surrounding plasma and endowed with one main and with two secondary plasma tori- and (b) PROTO-SPHERA -where the centerpost plasma terminates on electrodes and PF coils are contained inside the vacuum vessel. Two different colors distinguish the plasma of the main torus (ST) and of the surrounding plasma (SP). (c) 3D rendering of the PROTO-SPHERA plasma and of the annular electrodes.

equilibria, where μ is no longer constant on every flux surface, the surface averaged value of the relaxation parameter $\langle \mu \rangle = \mu_0 \langle \vec{j} \cdot \vec{B} / B^2 \rangle$ is therefore assumed to be injected from the external edge of the plasma to the internal axis of the main torus.

Appendix D illustrates that if open field lines are present in a configuration endowed with electrodes, such as in the case of PROTO-SPHERA, a relative magnetic helicity can still be well-defined and enjoys the same properties of magnetic helicity, as far as its flow and injection are concerned. Also, in appendix D and in figure D1, a Poynting-like theorem for the dynamics of the relative magnetic helicity in presence of electrodes is reported.

Since it is far from clear how an un-relaxed CKF equilibrium can be obtained in the laboratory, an experimental machine has been built in order to produce a plasma replicating the CKF equilibrium, as close as possible-, that is PROTO-SPHERA [1, 2, 12], which aims to investigate the study of these configurations. PROTO-SPHERA replaces the central part of the surrounding plasma (SP) of an un-relaxed CKF configuration by a centerpost plasma (CP) column in the form of a screw pinch, fed by electrodes internal to the vacuum vessel, and replaces the secondary plasma tori of an un-relaxed CKF by PF coils, internal to the vacuum vessel, see figures 2(a) and (b). The central screw pinch plasma impinges on two annular electrodes on top and bottom, see figure 2(c), and takes the shape of a plasma “mushroom” in front of both annular anode (top) and cathode (bottom).

PROTO-SPHERA can be regarded as restricting the SP of an un-relaxed CKF to the central screw pinch column only, or as enlarging the spherical tokamak configuration with metal centerpost to one with a CP, see figure 3(a). The PROTO-SPHERA experiment is quite different from spheromak configurations: spheromak plasmas are usually formed by kV

voltage magnetized coaxial plasma guns, used as helicity injectors, and are completely surrounded by a nearby conducting shell used as a stabilizer. PROTO-SPHERA is formed instead by the low voltage (80–300 V) breakdown of the central screw pinch plasma, thanks to the thermionic emission from the 2900 °C tungsten filaments that compose the annular cathode [13], see figure 1(c). PROTO-SPHERA furthermore (in all stages of its operations) never had a nearby conducting shell: the ST plasma is held in equilibrium by PF coils, just like a tokamak.

Such PF coils, internal to the vacuum vessel, are grouped into two sets, each composed of coils connected in series; PFInt-B group coils—the 4 + 4 coils shown in green in figures 3(b) and (c) shape the CP, mainly distributing the plasma discharge in three sections: on top the anodic CP; in the middle the main equatorial plasma (localized within a 0.87 m vertical space between the two PF2 poloidal field mirror coils) composed by the centerpost and the ST plasmas; on the bottom the cathodic CP. PFInt-A group coils—the 3 + 3 coils shown in red in figures 3(b) and (c) are compression coils in charge of containing the plasma torus. While the PFInt-A compression coils have a dipole moment opposite to the plasma torus dipole and could easily overturn the ST (the well known tilt mode of spheromak physics), the PFInt-B CP shaping coils have a larger dipole moment, which is aligned with the plasma torus dipole, a feature not present in any spheromak experiment. This novelty is what explains the remarkable stability obtained in the PROTO-SPHERA experimental plasmas.

Apart from this simplified consideration about the rigid tilt stability, the exact ideal MHD stability of the PROTO-SPHERA configuration has been assessed [14] by solving the eigenvalue problem in free-boundary mode, with the same code [15] used for the CKF configurations (see appendices B and C). The plasma beta limit depends upon the

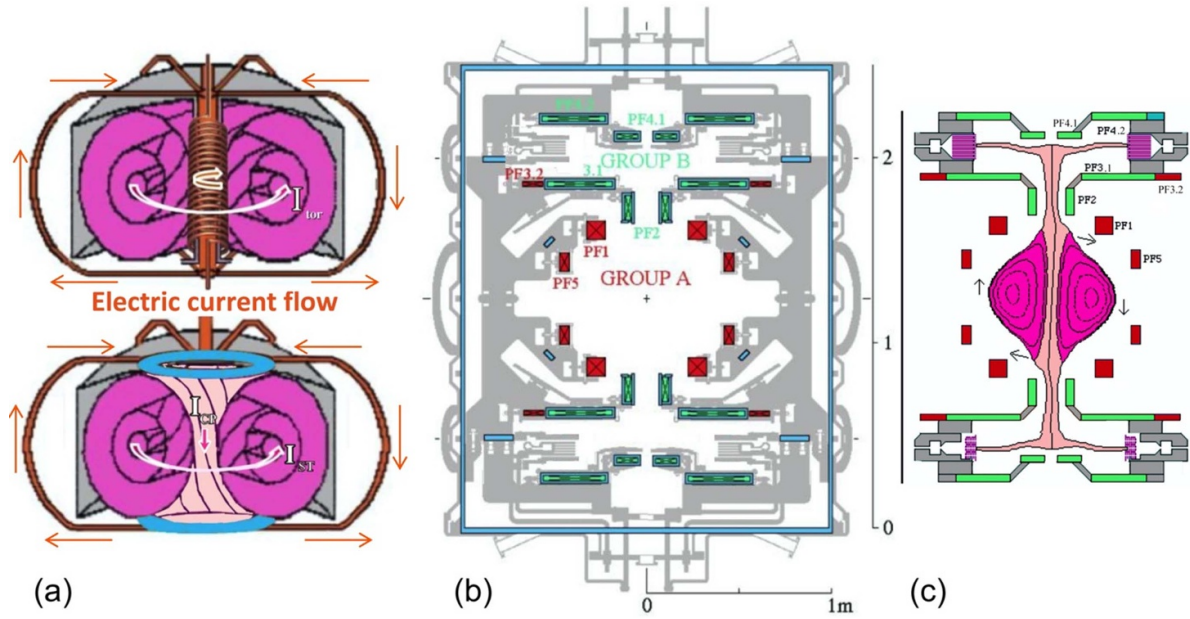


Figure 3. (a) Comparison between the scheme of a spherical tokamak (top) and that of PROTO-SPHERA (bottom). (b) The PF coils inside the vacuum vessel: the centerpost plasma shaping coils (Group B) are shown in green and the compression coils (Group A) in red. (c) A rigid tilt of the spherical torus of PROTO-SPHERA would be amplified by the Group A (red) PF coils, but would be further contrasted by the Group B (green) PF coils.

ratio between the ST current and the CP current I_{ST}/I_{CP} ; it goes from 21%–26% for ST/CP currents ratio in the range $I_{ST}/I_{CP} = 1$ down to 14%–16% for $I_{ST}/I_{CP} = 4$ (the range of variation -for the same ratio I_{ST}/I_{CP} - weakly depends upon the profiles inside the ST). In order to compare PROTO-SPHERA with a spherical tokamak with central rod, one can use the vacuum toroidal beta β_{T0} ($\beta_{T0} = 2\mu_0 \langle p \rangle_{vol} / B_{T0}^2$), where for the coupled ST + CP PROTO-SPHERA configuration B_{T0} means the toroidal field generated by the CP current I_{CP} on the geometric axis of the ST; with this somewhat artificial definition, the PROTO-SPHERA beta limit should be ranging from $\beta_{T0} = 28\%$ – 29% for $I_{ST}/I_{CP} = 0.5$, to $\beta_{T0} = 72\%$ – 84% for $I_{ST}/I_{CP} = 4$. Exact ideal MHD stability calculations confirm the simple rigid tilt stability consideration. By cutting shorter and shorter the CP, the overall configuration would be more and more destabilized [14].

In order to compare the performances of PROTO-SPHERA with plasma central screw pinch to those of a spherical tokamak with metal centerpost, geometrical size and plasma currents were chosen to be very similar to the ones of the pioneering spherical tokamak experiment START [16], operating- in Culham from 1991 to 1998, in particular, since the START vacuum vessel was kindly donated from UKAE-Culham to CR-ENEA Frascati. PROTO-SPHERA, with a CP column current $I_{CP} = 70$ kA, was designed to produce a ST of diameter $2 \bullet R_{sph} = 70$ cm and aspect ratio (major radius/minor radius) $A = 1.2 \div 1.3$, carrying a toroidal current $I_{ST} = 280$ kA. The small aspect ratio is linked to the amount of total toroidal current: the smaller the aspect ratio, the larger the current in the torus.

4. PROTO-SPHERA, construction and commissioning

The experimental program was divided into two steps: in Phase-1 the aim was just to obtain $I_{CP} = 10$ kA of CP current for 1 s, inside the START former aluminum vacuum vessel in the presence of the 4 + 4 PFInt-B group coils only, see figures 4(a) and (b). Since the beginning of the commissioning of PROTO-SPHERA, one problem was of paramount importance, that is, to adjust the boundary conditions of the experiment in order to avoid the possibility of the centerpost plasma current taking spurious paths.

The simple cylindrical geometry of the vessel allows for an easy access, thanks to which the experimental machine can be easily dismantled, removing the upper and lower parts independently, replacing or correcting any component inside the machine, and re-mounting it again. The boundary conditions of the experiment were therefore improved step-by-step, through a large number of repairs [2] (about 10 interventions over a 5-years span).

The commissioning started in 2015 and the aim of Phase-1 was achieved in 2018, when a CP at $I_{CP} = 10$ kA was routinely maintained for 1 s, first in argon, see figure 4(c), and then in hydrogen, see figure 4(d). The anode-cathode voltage V_e in argon plasmas was 90 V at break-down and ~ 200 V at the 10 kA flat-top. The argon line-averaged electron density $\langle n_e \rangle$ through the equator of the CP, measured by a 2-colors interferometer, was proportional to the centerpost current: $\langle n_e \rangle \propto I_{CP}$, reaching up to $\langle n_e \rangle \geq 4 \bullet 10^{20} \text{ m}^{-3}$ at $I_{CP} = 10$ kA [2]. The anode-cathode voltage V_e in hydrogen

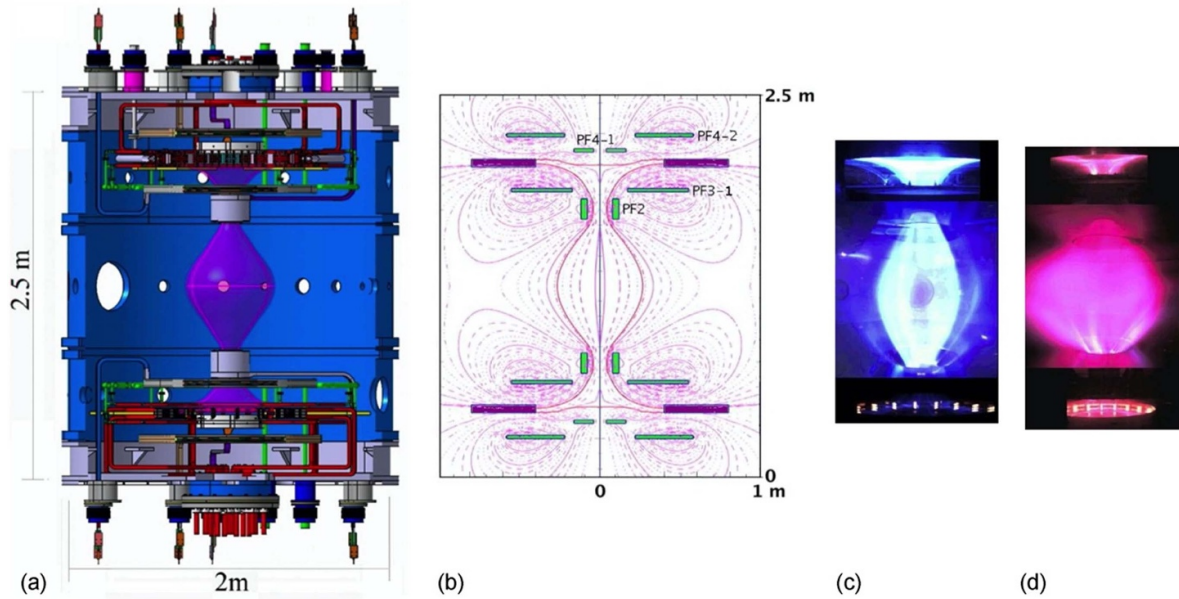


Figure 4. (a) The Phase-1 centerpost plasma sketched inside the START vacuum vessel, in the presence of 4 + 4 PF coils only. (b) Cross-sections of the magnetic configuration of Phase-1. (c) Visible image of the argon centerpost at $I_{CP} = 10$ kA. (d) Visible image of the hydrogen centerpost at $I_{CP} = 10$ kA. The plasma images are represented in true colors.

plasmas was 300 V at break-down and ~ 220 V at the 10 kA flat-top. The hydrogen line-averaged electron density through the equator of the CP reached up to $\langle n_e \rangle \geq 1.5 \cdot 10^{20} \text{ m}^{-3}$ at $I_{CP} = 10$ kA [2].

Phase-2 was supposed to begin as soon as Phase-1 objectives were successfully achieved in 2018: it had the aim of obtaining a ST with a toroidal current $I_{ST} = 280$ kA, while increasing the CP current from $I_{CP} = 10$ kA to $I_{CP} = 70$ kA and to maintain it for 1 s. Phase-2 was going to introduce inside the vacuum vessel the 3 + 3 further compression coils of the group PFInt-A, see figure 5(a). However, a quite different choice was made in 2019, that led to the need of an intermediate Phase-1.5, in order to verify that the torus could be formed. 3 + 3 PFInt-A provisional compression coils of figure 5(b) were in-house built and added inside the machine, while maintaining I_{CP} to 10 kA, the same level of Phase-1. 2 + 2 external compression poloidal field coils (dubbed PFExt) were introduced as well, outside the vacuum vessel. An insulating and transparent new vacuum vessel shown in figures 5(b) and (c) replaced the previous aluminum START vacuum vessel, in order to avoid skin currents and to allow for an immediate entrance inside the plasma of the vertical field generated by the external PFExt compression coils. Such setup demonstrated without any doubt that no nearby conducting shell is required for the plasma torus formation and sustainment in PROTO-SPHERA. Conical divertor plates were also introduced on top and bottom of the main plasma, in order to shield the internal PFInt-B shaping coils, shown in figure 4(b), from the power released by the anticipated magnetic reconnections. In Phase-1.5 the overall number of internal and external PF coils is therefore 18, fed by 3 different power supplies, including a new one based on super-capacitors. This arrangement allows for a considerable

flexibility of the experimental magnetic configurations. The first tori ($I_{ST} = 4$ kA, with $I_{CP} = 10$ kA) were immediately produced as soon as the 4 external PFExt compression coils (introduced in 2018) were energized with toroidal current opposite to the toroidal component of the current in the CP, even before the new insulating vessel was set up in 2019. In order to obtain a steady-state pre-existing magnetic field inside the experiment, a delay of about 0.6 s between the external PFExt energization and the plasma formation was therefore required in 2018, waiting for the decay of the reactive skin currents in the START aluminum vessel.

Tori were produced and sustained in all the following plasma campaigns, but this paper deals only with the evidence of tori gathered from the tomographic reconstruction, which will be described in the next section.

5. PROTO-SPHERA, tomographic diagnostic provides evidence of the torus

The diagnostics [2] used in Phase-1 were: a number of magnetic probes, a 2-color interferometer, a single 3600 fps visible light fast camera, visible and UV spectroscopy and a Langmuir probe. The introduction of the new insulating and transparent vacuum vessel in 2019 allowed for 3D tomographic diagnostic of the plasma visible light emission. Since 2019, 6 cameras (at 600 fps) were installed on the equatorial plane of the machine, forming equal angles of 60° between each other, and were attached to the transparent vacuum vessel, as shown in figure 6(a). Each of the 6 cameras is endowed with optics able to observe the whole of the main equatorial jet + torus plasma, as shown in figure 6(b), while the top anodic

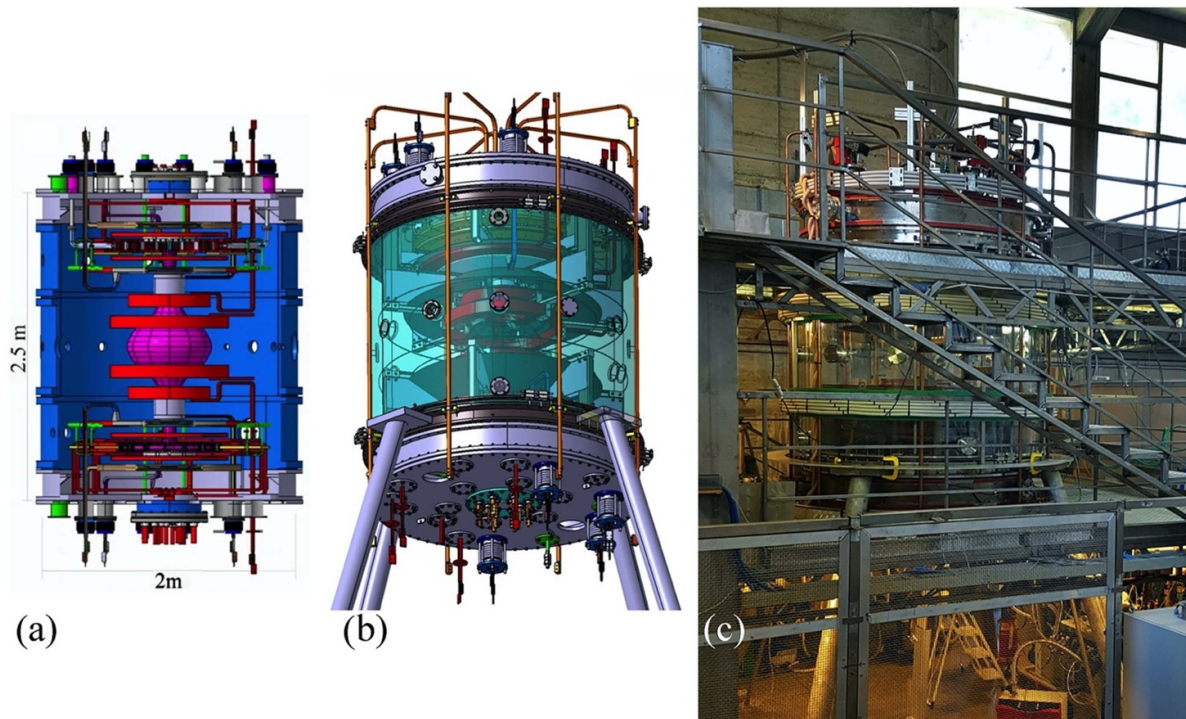


Figure 5. (a) The to-be-implemented Phase-2 centerpost + spherical torus plasma sketched inside the START vacuum vessel, in presence of 3 + 3 new PFIntA compression coils and of the old 4 + 4 PFIntB shaping coils of Phase-1. (b) 3D rendering of the experimental machine in its Phase-1.5 (after 2019), with the transparent vacuum vessel and the 3 + 3 provisional PFIntA compression coils (red); the conical divertor plates are shown in green-blue. (c) A picture of PROTO-SPHERA as it is after 2019, with transparent vacuum vessel, in order to show 3 of the 2 + 2 external poloidal field coils PFExt (grey), the bottom PFExt is hidden by the floor of the suspended platform.

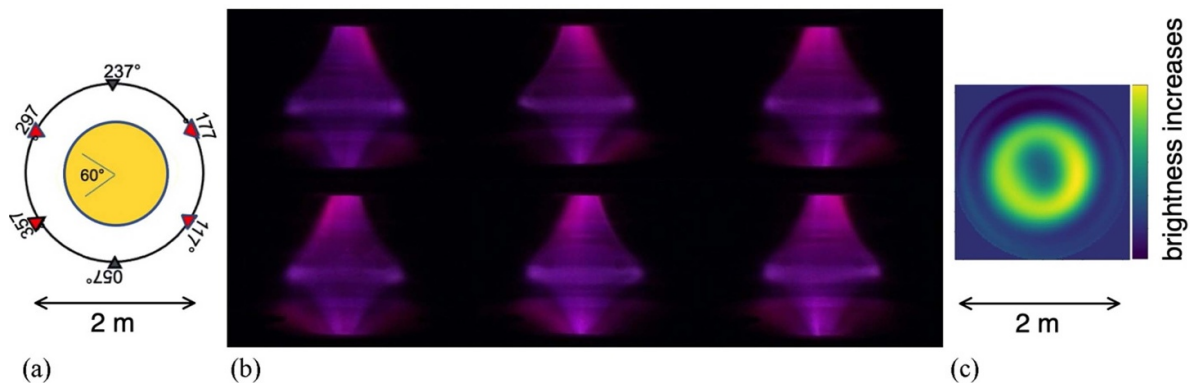


Figure 6. (a) The geometry of the 6 equally spaced (600 fps) cameras around the equator and immediately outside the transparent vacuum vessel, used for 3D visible light tomography. (b) The 6 images captured by the cameras at a given time instant, 57° – 357° in azimuthal (toroidal) angle, ordered top to bottom and left to right, during the initial formation of a hydrogen torus (true colors). (c) Tomographic reconstruction (false colors) on the equatorial plane of the plasma of PROTO-SPHERA, derived from such images.

and bottom cathodic mushrooms plasmas were vignettted by internal PFInt-B shaping coils as well as by the conical divertor plates. The first data were analyzed in 2019, but they were limited to the analysis of the equatorial plane of the plasma. The well-known analytical method devised by Cormack [17], which is based on Zernike polynomials [18], produced the first tomography of PROTO-SPHERA, just on the equator.

The presence of the torus in visible light emission was completely confirmed [19]; the reconstruction also indicated that the axial symmetry of the torus was slightly broken, see figure 6(c). The torus shown in figure 6(b) was obtained in

2019, with the help of PFExt external compression coils alone, and was very small in size since it was a torus with quite a large aspect ratio ($R/a \sim 6$ –8).

In the following year 2020 much larger tori, up to smaller aspect ratios $R/a \sim 4$, were obtained, like that of the helium discharge shown in figure 7(a). In order to reach that size, both PFExt external compression coils as well as the PFInt-B provisional compression coils were energized at the same time with independent currents.

Such tori were pulsating plasma objects and their pulsations showed the first evidence of magnetic reconnections: plasma

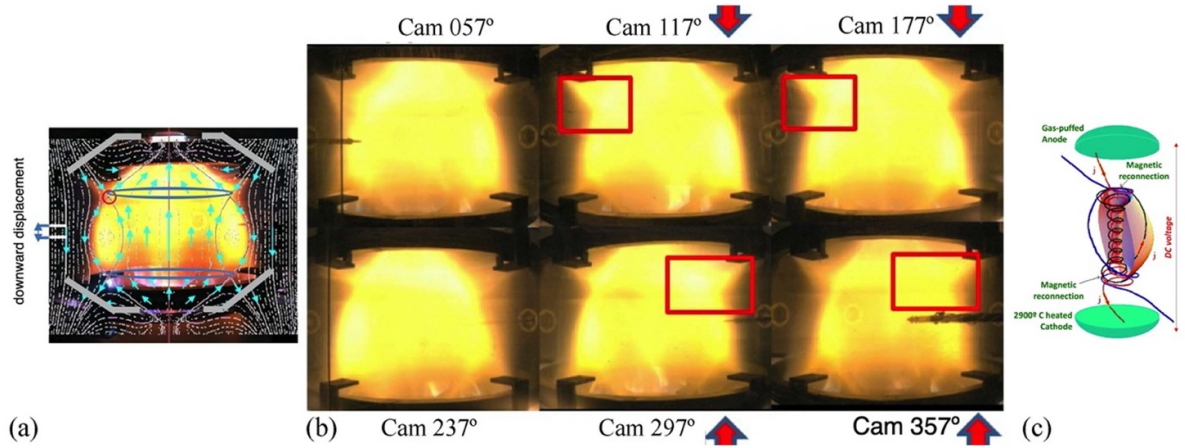


Figure 7. (a) A helium plasma torus obtained in 2020 (true colors), with the help of external PFExt and internal PFInt-A compression coils; the plasma is slightly shifted towards the bottom of the machine, so that the upper circle of X-points is better visible than the lower circle. The direction of the field is shown with cyan arrows. (b) The visible light effects of a pulsation (reconnection), as observed from the 6 tomographic cameras in azimuthal (toroidal) angle, appears only on 4 of them. (c) A sketch of the reconnection mechanism.

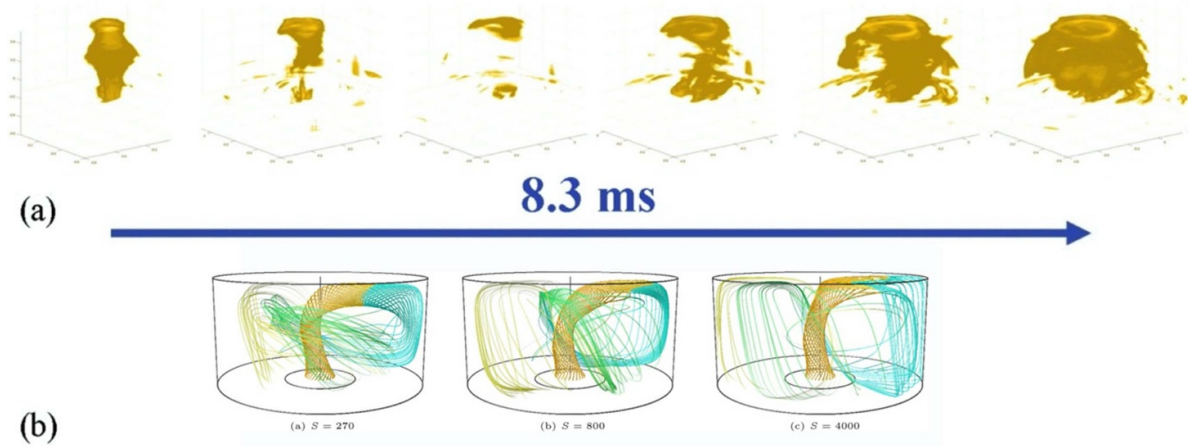


Figure 8. (a) 3D tomographic reconstruction of the visible light emission density observed by the 6 cameras at 60 fps (false color) of the formation of the helium discharge shown in figure 7. (b) PROTO-SPHERA formation, as predicted from R. Farengo *et al*, as a function of the Lundquist number $S = \tau_R/\tau_A$, ratio between the current diffusion time τ_R and the Alfvén time τ_A , respectively 1–10 ms and 0.5 μ s in present PROTO-SPHERA plasma. Reprinted from [24], with the permission of AIP Publishing.

brightening of divertor tails and deformation of the plasma in the area of the X-points. Such phenomena were not diffused all over the circles of ordinary X-points, but were limited to toroidal arcs of less than 60° along such circles, see figure 7(b), indicating the non-axisymmetric nature of the magnetic reconnections in PROTO-SPHERA, as sketched in figure 7(c).

Since in PROTO-SPHERA the helicity source (the CP) is magnetically separated but adjacent to the helicity sink (the ST), resistive MHD instabilities produce a helicity flow from the centerpost, with a larger μ_{CP} , to the torus with a smaller μ_{ST} (see also appendix D). In the intermediate Phase-1.5 of the experiment the current in the CP is still limited to $I_{CP} = 10$ kA (the same value as in Phase-1), whereas the shaping magnetic field B_{CP} produced by the PFInt-B coils has remained, since Phase-1, at its full Phase-2 value. In Phase-1.5 the too low relaxation parameter $\mu_{CP} \propto j_{CP}/B_{CP}$ allows for a current in the ST which is only one half of the current in the CP: $I_{ST}/I_{CP} \sim 1/2$. Consequently, the aspect ratio of the torus has

never been smaller than $R/a \sim 4$. Phase-2, while pushing to $I_{CP} = 70$ kA, should allow for $I_{ST}/I_{CP} \sim 4$ and should decrease the aspect ratio of the ST towards 1.

To obtain a full 3D tomographic reconstruction of the visible light emission, an extension to 3D of the well-known method of Radon transform [20–22] was carried out. In fact, a typical approach to 3D image reconstruction is 2D computed tomography, which reconstructs the sought image based on a set of slice projections, relying on the Fourier slice theorem in 2D. Instead, we developed an imaging technique based on the Fourier slice theorem in 3D, which relates a set of projections onto planes, that are a 3D Radon transform, to a 3D Fourier transform. The set of projections of visible light emission onto planes are the pictures themselves provided by the six cameras. By calculating 3D inverse Fourier transforms, we could reconstruct the 3D image of the plasma emission [23]. From this 3D numerical analysis novel and relevant information was derived. In particular figure 8(a) reports the density

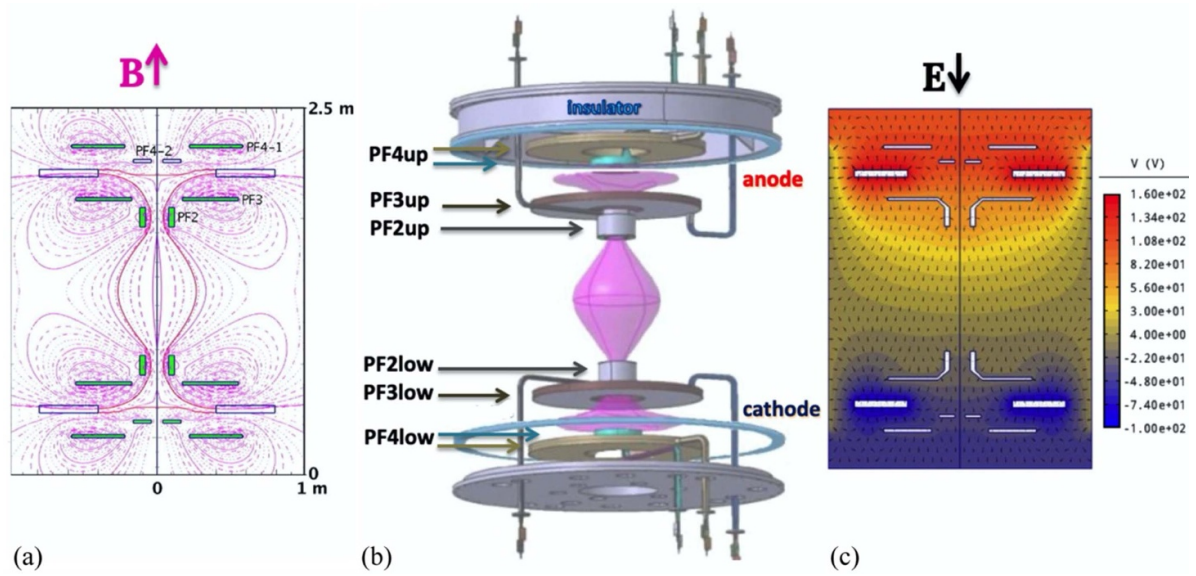


Figure 9. (a) The up/down even-symmetric magnetic field present inside the machine, shown by flux surfaces cross-sections. (b) The internal PFInt-B shaping coils are up/down even-symmetric; electrodes are indicated but not shown. (c) The vacuum electrostatic potential as calculated from all the charged metallic surfaces (electrodes and PF coils), which is not up/down odd-symmetric.

of light emission reconstructed at six different time instants in 3D. It displays the physics of the formation of the torus, which happens in about 5–8 ms since the centerpost plasma current I_{CP} had started-up and continued to grow towards $I_{CP} = 10$ kA, in a completely static pre-existing field produced by external (PFExt) and internal field coils (PFInt-A and PFInt-B). The plasma torus grew from a kinked filament, due to the destabilization of the CP. This observation aligns well with the predictive calculations carried out by the group of Ricardo Farengo, as shown in figure 8(b) [24].

Figure 7(a) shows that the helium plasma on top of the upper circle of X-points (the circle nearest to the anode) is particularly bright; this feature corresponds to the fact that the torus has slightly but permanently drifted downward (by 3÷4 cm) from the equator of the machine, towards the lower (cathodic) side. These two effects are presumably associated with the electrostatic odd-symmetry breaking about the equatorial plane. The plasma charges electrostatically all conductors (PF coils, divertor plates) present inside the vacuum vessel, and even if the magnetic field \vec{B} is up/down even-symmetric, as shown in figure 9(a), each metal surface like the internal PF coils, shown in figure 9(b), charges at a specific electrostatic potential, which is not up/down odd-symmetric. While the total potential difference V_e is obviously applied between anode and cathode, as soon as the CP current I_{CP} starts growing, the anode (on top) charges at a positive value that is 60% higher than the absolute value of the negative potential of the cathode (on bottom). The zero electrostatic potential contour is therefore much nearer to the cathode than to the anode, not far from the PF2low mirror coil of figure 9(b).

This remains true in all gases used for plasma production (argon, helium and hydrogen) and seems to be the reason why the main plasma rotates azimuthally (toroidally) in all cases,

irrespective of the kind of discharge (either a pure centerpost discharge or a discharge endowed with a torus around the centerpost). The direction of rotation of the main plasma is clockwise (viewed from the top) at an angular frequency $\omega_{Tor} \sim 500 \div 600$ rad s^{-1} , and seems to be coherent with the anodic direction of $\vec{E} \wedge \vec{B}$, which is predominant in the main plasma region, between the PF2up and the PF2low of figure 9(b).

Not only does the plasma rotate, but it also has a slightly oval shape. This is shown in figure 10, which indicates that all the visible light cameras exhibit a clear correlation between total brilliance and diameter of the plasma in the equatorial plane.

Rotation and ovalization of plasma are further confirmed by the 3D tomographic reconstructions of light emission density, that show that the plasma torus acts as a slightly oblique rotator, as displayed in figure 11. This behavior, on top of the presence of jets and torus, indicates another analogy with the PWN morphology: Pulsars, born spinning, provide energy to their Nebulae, acting as braked oblique rotators

6. PWN and CKF up/down odd force-free field

The central engine of a PWN is a bright Pulsar (~ 10 km radius), endowed with a strong dipolar magnetic field, which was the original magnetic field of the progenitor star, amplified by the gravitational collapse that gave birth to the Pulsar. The rotational speed of the progenitor star was amplified as well during the collapse. An induced electric field $\vec{E} = -\vec{V} \wedge \vec{B} = -(\vec{\Omega} \wedge \vec{R}) \wedge \vec{B}$, like the one created by a rotating Faraday disk [25], produces a potential difference between the poles and the equator of the Pulsar, which becomes polarized. A surface

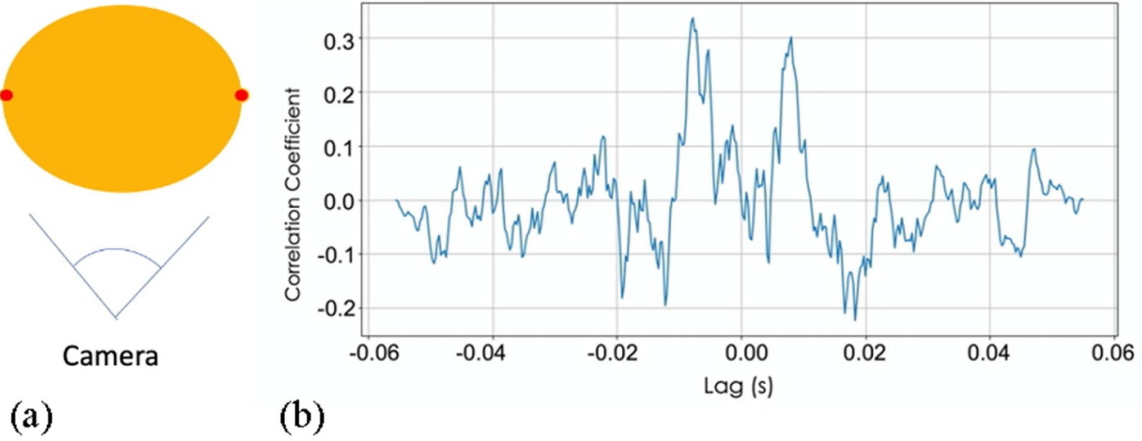


Figure 10. (a) The view of the plasma from any of the visible light cameras (ovalization is more enhanced than in real life). (b) The correlation coefficient (in term of the time lag, in seconds) between the total brilliance and the measured diameter of the plasma, as observed by a visible light camera.

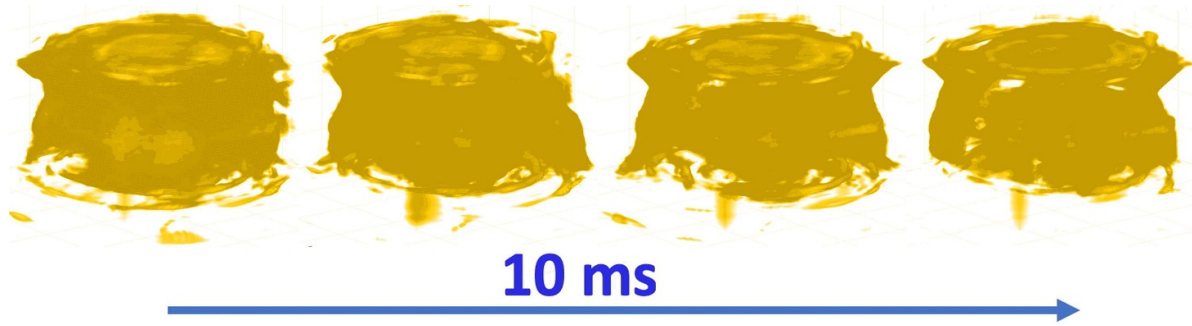


Figure 11. Four times instants of the 3D tomographic visible light emission density reconstruction of a PROTO-SPHERA helium discharge endowed with torus (false color). 10 ms period more or less corresponds to one full rotation.

electric field raises charged particles from the star, with an associated e^+/e^- couples production, so that an electrically conducting atmosphere is formed, and mostly composed, near the Pulsar, by the e^+/e^- couple plasma. Such plasma wind is frozen into the rotating field of the Pulsar and its rotational speed increases until it reaches the speed of light at the light cylinder (~ 5000 km radius). Outside the light cylinder the magnetic field lines open and their winding implies a radial Poynting flux, which is the origin of the magnetic braking of the Pulsar. The braking is enhanced if the Pulsar has a magnetic dipole axis which is misaligned with respect to the rotation axis. The usually oblique rotator provides energy to the whole PWN, whose plasma extends to few light years distance, much beyond the light cylinder. The PWN is continuously replenished by e^+/e^- couple plasma moving at relativistic speed; such a wind downstream impinges on the Pulsar Ejecta, develops shock waves and is enriched by ions. The observed spectrum of electromagnetic emission from the PWN extends beyond the PeV (10^{15} eV) energy, showing evidence of particle acceleration, as the photon energies extend from x-rays up to γ -rays. The best known example of a natural accelerator in the Galaxy is the Crab Nebula, and it is in fact highly efficient, since more than the 25% of its released rotational power is emitted in radiation.

The most popular model used to describe the flow of electric current in a PWN is the *ffmf* proposed by Michel [26], termed the “split-monopole” and indicates current density flowing out of the equator and closing the electric circuit with current density returning in both jets, although it expresses purely radial currents. A tentative scheme that describes the PWN, while encompassing the geometry of jets and tori, can be obtained superposing two axisymmetric homogeneous *ffmfs*, each with $\nabla \wedge \vec{B} = \mu \vec{B}$, both having the same value of the relaxation parameter $\mu = \mu_0 \vec{j} \cdot \vec{B} / B^2$. The first *ffmf*, see figure 12(a), is the up/down odd-symmetric Chandrasekhar-Kendall force-free field [9] of order-2, which in spherical geometry (r, ϑ, φ) admits the poloidal flux function: $\psi_\mu^{\text{CK,odd}}(r, \vartheta) = -(\mu r) j_2(\mu r) \sin \vartheta P_2^1(\cos \vartheta)$, where $j_2(\mu r)$ is the second order spherical Bessel function, having its m th radial zero at $(\mu r) = x_{2,m}$ and $P_2^1(\cos \vartheta)$ is the Legendre polynomial of order 2. The second *ffmf*, see figure 12(b), is the up/down odd-symmetric Furth square-toroid force-free field [10], which can be written as: $\psi_{\mu\lambda}^{\text{F,odd}}(r, \vartheta) = \sqrt{\mu^2 - \lambda^2} r \sin \vartheta J_1(\sqrt{\mu^2 - \lambda^2} r \sin \vartheta) \sin(\lambda r \cos \vartheta)$ for any value of $\lambda < \mu$, where J_1 is the cylindrical Bessel function of order 1. Figures 12(a) and (b) show the upper ($Z > 0$) part of both *ffmfs*.

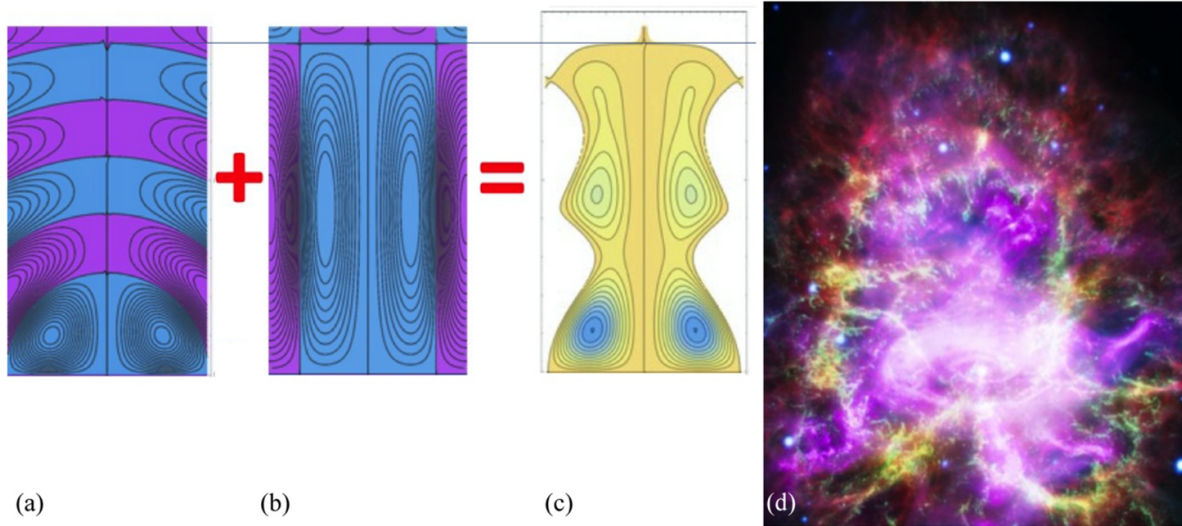


Figure 12. (a) Cross-sections of the upper ($Z > 0$) part of Chandrasekhar–Kendall (CK) odd-symmetric $ffmf$ $\psi_{\mu}^{CK,odd}$ with relaxation parameter $\mu = x_{2,6} = 21.85387$. (b) Cross-sections of the upper ($Z > 0$) part of Furth square toroid (F) odd-symmetric $ffmf$ $\psi_{\mu\lambda}^{F,odd}$ with same μ and zero-matching parameter $\lambda = (\pi \bullet x_{2,6})/x_{2,5} = 3.6736$ at the fifth zero of the CK $ffmf$. (c) Cross-sections of the upper ($Z > 0$) part of the poloidal flux function of the odd-symmetric CKF force-free fields: $\psi_{\mu\lambda}^{CKF,odd}(r, \vartheta) = \psi_{\mu}^{CK,odd} + \gamma \psi_{\mu\lambda}^{F,odd}$, with constant superposition coefficient $\gamma = 0.405$, detailing its composition in terms of different plasma regions, divided by a magnetic separatrix; (d) Composite (x-ray, UV, Visible, IR and Radio) image of the Crab Nebula. Reproduced with permission from [27]. Credit: NASA, ESA, J. DePasquale (STScI), and R. Hurt (Caltech/IPAC).

A simply connected $ffmf$ can be obtained by superimposing, through a constant coefficient γ , the two solutions $\psi_{\mu}^{CK,odd}$ and $\psi_{\mu\lambda}^{F,odd}$ with the same μ : $\psi_{\mu\lambda}^{CKF,odd}(r, \vartheta) = \psi_{\mu}^{CK,odd} + \gamma \psi_{\mu\lambda}^{F,odd}$. The relaxation parameter is chosen as $\mu = x_{2,6} = 21.853874$, so that within a unitary circle six zeroes of $\psi_{\mu}^{CK,odd}$ are present in the Chandrasekhar–Kendall field. The zero-matching parameter λ of the Furth square toroid field is chosen as: $\lambda = x_{2,6}\pi/x_{2,5} = (21.853874 \bullet \pi)/(18.689036) = 3.6736$, so that at $R = 0$, $Z = x_{2,5}/x_{2,6} = 18.689/21.8538 = 0.85518$ the zeroes of $\psi_{\mu\lambda}^{F,odd}$ and of $\psi_{\mu}^{CK,odd}$ coincide. This kind of a “number of zeroes” rule on the zero-matching parameter λ helps in obtaining, near to the origin ($R = 0$, $Z = 0$), a simply connected and closed magnetic field configuration, with a unique sign of the toroidal components of j_{φ} and B_{φ} .

By choosing odd–even zeroes in an increasing sequence, more and more extended jets can be obtained. Figure 12(c) shows the upper ($Z > 0$) part of such superposition, with constant superposition coefficient $\gamma = 0.405$; the choice of the matching condition at the 5th–6th zeroes has been derived by trying to fit the aspect ratio between the extensions of the vertical jet and of the horizontal torus observed in the Crab Nebula, see figure 12(d).

Such superposition of up/down odd-symmetric $ffmf$ s with the same μ cannot however fit the real up/down mixed symmetry of a PWN: the continuity of the $\vec{B}_{vertical}$ field direction in the jets of the 2 hemispheres is inherited by the dipolar field of the Neutron Star; the Faraday disk effect gives instead opposite $\vec{j}_{vertical}$ in the jets of the 2 hemispheres. Summing 2 odd-symmetric CK + F $ffmf$ s with the same μ would give opposite $\vec{B}_{vertical}$ on the 2 hemispheres, which is not correct. In fact, the only way of satisfying both conditions is the juxtaposition of two superpositions $\psi_{\mu\lambda}^{CKF,odd}(r, \vartheta) = \psi_{\mu}^{CK,odd} +$

$\gamma \psi_{\mu\lambda}^{F,odd}$, but with opposite μ : like $\mu > 0$, $\gamma > 0$ on the upper and $-\mu < 0$, $-\gamma < 0$ on the lower hemisphere, as shown in figure 13. Juxtaposition of two $ffmf$ s with opposite μ and γ can provide magnetic configuration endowed with magnetic discontinuities [28]. In cylindrical coordinates (R, ϕ, Z) the full form of the solution for the PWN axisymmetric flux function, with the choices $\mu > 0$, $\gamma > 0$ for $Z > 0$ and $-\mu < 0$, $-\gamma < 0$ for $Z < 0$, is:

$$\psi_{\mu\lambda}^{PWN}(R, Z) = \frac{RZ}{|Z|} \left[-|\mu| j_2(|\mu|r) P_2^1\left(\frac{Z}{\sqrt{R^2 + Z^2}}\right) + |\gamma| \sqrt{\mu^2 - \lambda^2} J_1\left(\sqrt{\mu^2 - \lambda^2} R\right) \sin(\lambda Z) \right],$$

for the toroidal (azimuthal) field:

$$B_{\phi}^{PWN}(R, Z) = \frac{|\mu|}{2\pi} \left[-|\mu| j_2(|\mu|r) P_2^1\left(\frac{Z}{\sqrt{R^2 + Z^2}}\right) + |\gamma| \sqrt{\mu^2 - \lambda^2} J_1\left(\sqrt{\mu^2 - \lambda^2} R\right) \sin(\lambda Z) \right].$$

and for the poloidal field components:

$$B_{R\mu\lambda}^{PWN}(R, Z) = -(\partial \psi_{\mu\lambda}^{PWN} / \partial Z) / (2\pi R),$$

$$B_{Z\mu\lambda}^{PWN}(R, Z) = +(\partial \psi_{\mu\lambda}^{PWN} / \partial R) / (2\pi R).$$

This implies opposite directions of the toroidal field $B_{\phi}^{PWN}(R, Z)$ on the 2 hemispheres, but inside the main tori the flux function $\psi_{\mu\lambda}^{PWN}(R, Z)$ is positive in both upper and lower hemispheres, which means that the toroidal current density $j_{\phi}^{PWN}(R, Z)$ is positive in both tori near the equator. The azimuthal (toroidal) field $B_{\phi}^{PWN}(R, Z)$ is null on the equator, positive inside the upper torus, but is negative inside the lower torus; the same signs of $B_{\phi}^{PWN}(R, Z)$ apply to both jets, since

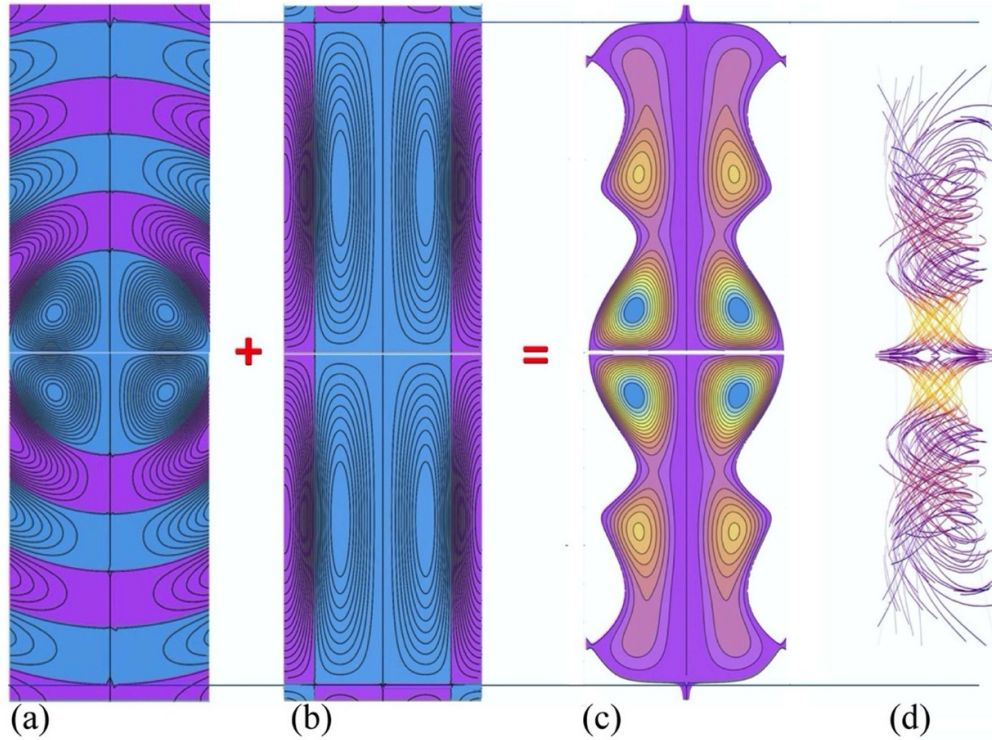


Figure 13. (a) Cross-sections of the upper part ($Z > 0$) part of Chandrasekhar–Kendall (CK) *ffmf* $\psi_{\mu}^{\text{CK, odd}}$ with relaxation parameter $\mu = x_{2,6} = 21.8538$, juxtaposed with the lower ($Z < 0$) part, but with $\mu = -x_{2,6} = -21.853874$. Flux function has up/down even-symmetry and is null on the equator. (b) Cross-sections of the upper part ($Z > 0$) of Furth square toroid odd *ffmf* $\psi_{\mu\lambda}^{\text{F, odd}}$ with $\mu = x_{2,6} = 21.853874$ and zero-matching parameter $\lambda = (\pi \bullet x_{2,6}) / x_{25} = 3.6736$, juxtaposed with lower part ($Z < 0$), but with $\mu = -x_{2,6} = -21.853874$ and $\lambda = (\pi \bullet x_{2,6}) / x_{25} = 3.6736$. Flux function is up/down even-symmetric and is null on the equator. (c) Cross-sections of the upper part ($Z > 0$) of the PWN *ffmf* model flux function: $\psi_{\mu\lambda}^{\text{PWN}}(r, \vartheta) = \psi_{\mu\lambda}^{\text{CKF, odd}}(r, \vartheta) = \psi_{\mu}^{\text{CK, odd}} + |\gamma| \psi_{\mu\lambda}^{\text{F, odd}}$, juxtaposed with lower part ($Z < 0$): $\psi_{\mu\lambda}^{\text{PWN}}(r, \vartheta) = \psi_{-\mu\lambda}^{\text{CKF, odd}}(r, \vartheta) = \psi_{-\mu}^{\text{CK, odd}} - |\gamma| \psi_{-\mu\lambda}^{\text{F, odd}}$, both with constant superposition coefficient $\gamma = 0.405$. (d) Field-line-tracing of PWN *ffmf* model, enlarged near the origin in order to show the current layer present on the equator. Geometric scale is such that 6 zeroes of the CK *ffmf* are contained in a unitary sphere.

they are surrounded by each torus. In the jets inside the tori the vertical field $B_{Z\mu\lambda}^{\text{PWN}}(R, Z)$ has up/down even-symmetry, and it is positive in both hemispheres. The only discontinuity that appears on the equator is the one of the radial field $B_{R\mu\lambda}^{\text{PWN}}(R, Z)$: it has opposite values on any point R on the upper ($Z > 0$) and lower ($Z < 0$) sides of the equator, that is negative on the equator in the upper hemisphere, and positive on the equator in the lower hemisphere. The $\psi_{\mu\lambda}^{\text{PWN}}(R, Z)$ model of a PWN gives rise to a radial B_R magnetic discontinuity and implies a singular toroidal j_{ϕ} current density layer on the equator of the PWN at $Z = 0$, which is in agreement with the well-known ‘split-monopole’ model [26].

The symmetries of the plasma current densities \vec{j}^{PWN} , are opposite to the symmetries of the fields \vec{B}^{PWN} . This is due to $\mu > 0$ in the upper hemisphere, $\vec{j}^{\text{PWN}} = (\mu/\mu_0) \vec{B}^{\text{PWN}}$; and to $\mu < 0$ in the lower hemisphere, $\vec{j}^{\text{PWN}} = (-|\mu|/\mu_0) \vec{B}^{\text{PWN}}$. In the upper hemisphere the directions of \vec{j}^{PWN} are the same as those of \vec{B}^{PWN} , while in the lower one the directions of \vec{j}^{PWN} are the opposite to those of \vec{B}^{PWN} . The poloidal plasma current density $j_{\text{pol}}^{\text{PWN}}$ enters the equator between the two tori and exits from both jets. The signs of all fields and currents must obviously be reversed if the opposite choice $-|\mu| < 0$, $-|\gamma| > 0$ for $Z > 0$ and $\mu > 0$, $\gamma > 0$ for $Z < 0$ is adopted.

Although the composite-wavelength image of the Crab Nebula, shown in figure 14(a), does not exhibit an evident double torus and the polarimetric radio [29] and x-ray [30] observations show a dominant toroidal field direction, the vertical component of the magnetic field observed in radio emission, shown in figure 14(b), shows some resemblance to the field-line-tracing obtained from the *ffmf* $\psi_{\mu\lambda}^{\text{PWN}}(R, Z)$ model of figure 14(c). No perspective correction has been attempted on the field line tracing model of figure 14(c).

The observation of another PWN, the Vela Nebula [31], enables instead a clear observation of a double torus, see figure 15(a). The double torus model was put forward in the literature since 2004 [32]. The tilt angle of the direction of observation with respect to the axis of the Vela Nebula is not completely certain, but it is more pronounced than in the previous case of the Crab Nebula. Therefore the comparison with the $\psi_{\mu\lambda}^{\text{PWN}}(R, Z)$ flux surface *ffmf* model has been roughly corrected by reducing by a factor 2 the aspect ratio between the total length along the jets and the tori horizontal dimensions, see figure 15(b). Recent polarimetric x-ray [33] observations from the IXPE satellite show a dominant toroidal field direction, which extends far beyond the brightest x-ray emission region.

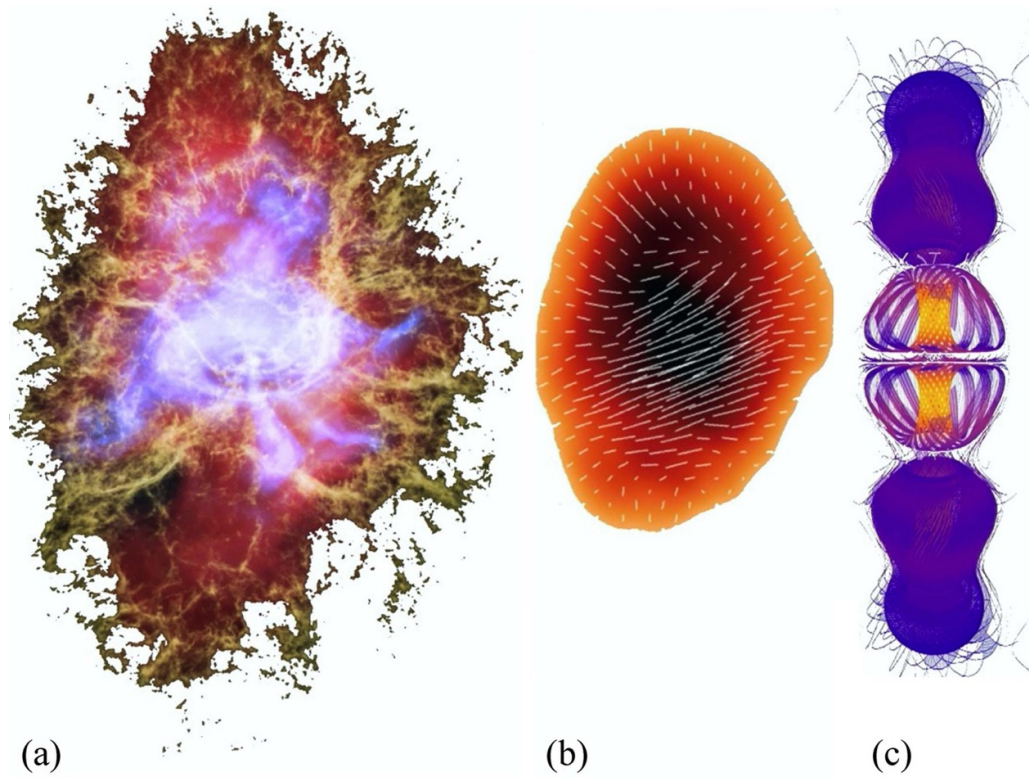


Figure 14. Crab Nebula. (a) Composite (x-ray, UV, Visible, IR and Radio) image of the Crab Nebula [27], Credits: NASA, ESA, J. DePasquale (STScI). (b) B-field direction from radio emission [29]. (c) Field-line-tracing B field of PWN, from $\psi_{\mu\lambda}^{\text{PWN}}(R, Z)ffmf$ model; no attempt to correct for tilted direction of observation has been done. Reproduced with permission from [27]. Credit: NASA, ESA, J. DePasquale (STScI), and R. Hurt (Caltech/IPAC). Reproduced with permission from [29].

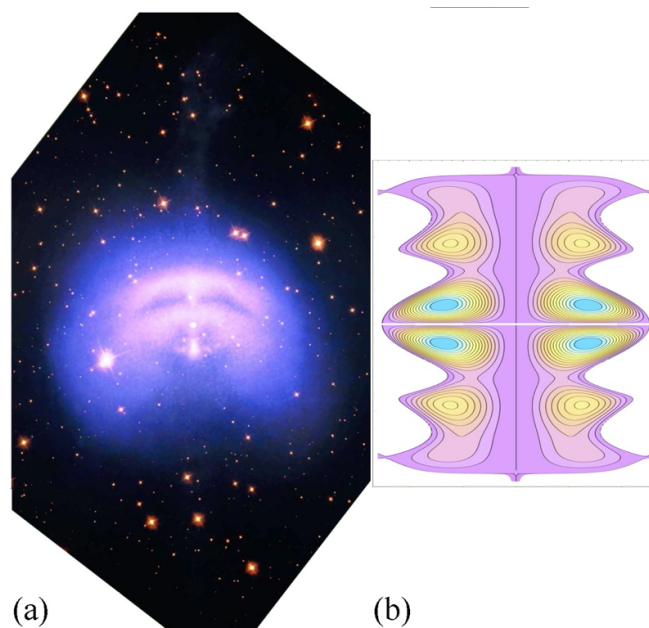


Figure 15. Vela Pulsar Wind Nebula. (a) Merged Chandra image, where the tilted perspective is uncertain, but evident [31]. (b) The PWN $\psi_{\mu\lambda}^{\text{PWN}}(R, Z)ffmf$ model: in order to match the tilted direction of observation, it has been naively corrected by shortening by a factor of 2 the vertical dimension of the flux surface plot of figure 13(c). Reproduced from [31]. © IOP Publishing Ltd All rights reserved.

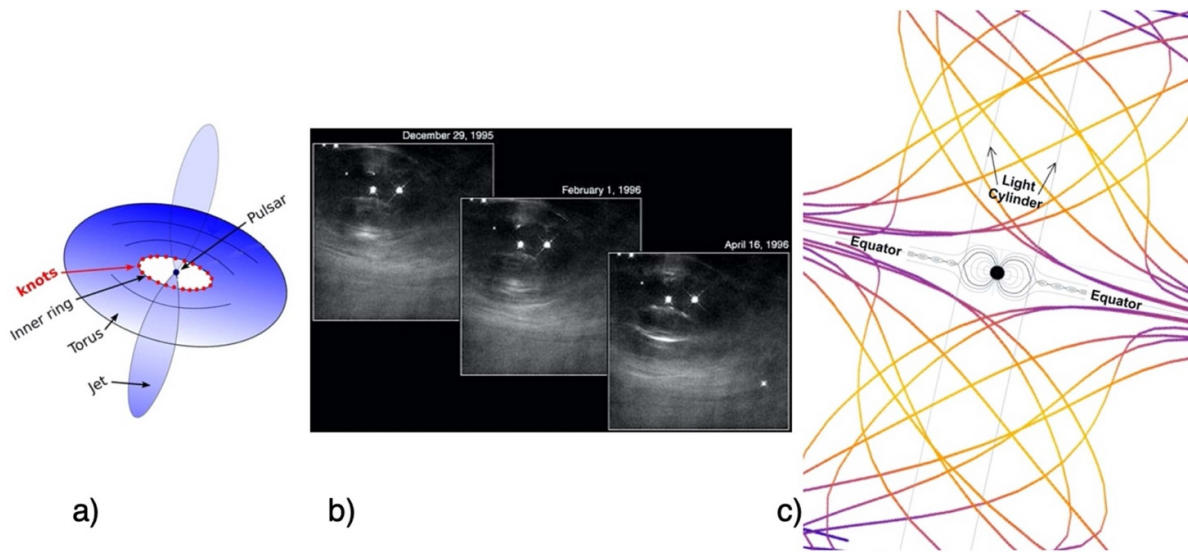


Figure 16. (a) Scheme of equatorial plane of jets + torus of the Crab PWN, with position of fast-moving knots evidenced. Reproduced from CC BY 4.0. [34]. (b) Hubble Space Telescope visible image of fast-moving knots [35, 36], Reproduced with permission from <https://hubblesite.org/contents/media/images/1996/22/429-Image.html?news=true>. Credit: Jeff Hester and Paul Scowen. (c) Scheme of reconnecting plasmoid chain [37] between the two tori, displayed on the equator, just outside the light cylinder of the Pulsar, shown inside the field-line-tracing of the $\psi_{\mu\lambda}^{PWN}(R, Z) fmf$ model of figure 13(d). Reproduced from [37]. © 2014. The American Astronomical Society. All rights reserved.

The question of the origin of the acceleration of particles in the PWN remains unsettled; the main competing ideas are Fermi-type acceleration in shockwaves and magnetic reconnection. If magnetic reconnections are responsible for the acceleration, the PWN $\psi_{\mu\lambda}^{PWN}(R, Z) fmf$ model indicates a region where magnetic reconnections should be apparent, which is the equatorial region, where both the radial and the toroidal magnetic fields are opposite. Should any deviation from *fmf* configuration occur, the two neighboring tori would furthermore be attracted against one another, since the toroidal currents in both of them are oriented in the same direction (contrary to the toroidal magnetic field). A singular current layer on the equatorial plane, where both the radial and the toroidal magnetic fields change sign, can give rise to reconnecting plasmoids. Such a powerful reconnection machine can be operated between the two tori on the equatorial plane of a PWN, sketched in figure 16(a) [34]. It is further suggested by the Hubble observation of fast-moving bright ‘knots’ [35, 36], shifting at large fractions of the speed of light (up to $c/2$) on the inner equatorial plane of the Crab PWN, shown in figure 16(b). These knots could be interpreted as reconnection events involving plasmoids on the equatorial plane [37], see figure 16(c).

7. Conclusions

Jet + torus linear force-free fields (*fmf*) can describe PWNe and can be reproduced in laboratory experiments such as PROTO-SPHERA. The CKF *fmf* configuration, endowed with up/down even-symmetry, with respect to the equatorial plane (see appendix B), has been the basis upon which the PROTO-SPHERA was designed as a feasible laboratory experiment and built as a centerpost + torus configuration. The

experiment successfully demonstrated that the jet + torus configuration can be routinely formed and sustained in the laboratory for as long as the central plasma jet is kept running by the power supplied to the electrodes, that is 1 s. This plasma duration is limited by the inertial (passive) power removal. The choice to conduct the experiment in such a way was due to the necessity of building a low-cost explorative experiment, without engineering complications connected to active power removal. The duration of 1 s is nevertheless much longer than both relevant plasma time scales, that are the Alfvén time, which is $1/2 \mu s$, and the current diffusion time, which is at the moment 1 to 10 ms. So, from the point of view of plasma physics alone, in this case, 1 s is perfectly equivalent to the sustainment of the jet + torus plasma in steady-state. The plasma obtained in PROTO-SPHERA matches well with design calculations: it is quite stable in ideal MHD, even in the absence of any conducting shell near the plasma. A novel diagnostic, the 3D tomographic reconstruction of the visible light emitted by the plasma, shows that magnetic reconnections form and sustain the torus; they are not axisymmetric phenomena; their places of occurrence are the two circles of ordinary X-points on top and bottom of the equator. The experiment shows that magnetic reconnections are recurring and that the magnetic flux transfers from the centerpost to the torus are efficient enough. The energy transfer is likely to become more efficient, when the plasma currents will be increased by about an order of magnitude in the to-be-implemented Phase-2 of the experiment.

PROTO-SPHERA also enabled for the following novel observations:

- The plasma rotates in toroidal direction, certainly a stabilizing feature for all magnetic confined plasmas.

- The torus is formed in a purely pre-existing magnetostatic field (indicating the possibility of obtaining axisymmetric magnetic confinement traps composed by permanent magnets only).
- The PROTO-SPHERA plasma is finally an oblique rotator, just as the plasma of PWNe.

A different model, with similarities to the one previously mentioned, has been set-up in order to describe the Pulsar Wind Nebulae, which is the odd symmetric CKF configuration endowed with opposite relaxation parameter $\mu/|\mu|$ with respect to the equatorial plane. The difference is that in the PWN *ffmf* model the current in the plasma jets has opposite directions in the 2 hemispheres, whereas in PROTO-SPHERA the plasma current goes through the center of the magnetic configuration without changing direction. The main variant with respect to the laboratory experiment is that in the astrophysical model two tori are present, one above and the other below the equator. Even if deviations from the *ffmf* configuration should appear, these two tori would continue to remain in position due to the attraction force between their toroidal currents, which both flow in the same direction, despite opposite radial and toroidal fields on the two sides of the equator, where a singular toroidal (azimuthal) current layer forms. The *ffmf* model of the PWN configuration appears to be an impressive reconnection machine: the place of occurrence of the magnetic reconnection seems to be the equator, where bright fast-moving not-axisymmetric knots have been observed.

The two cases (laboratory and astrophysics) are therefore quite distinct, both in the number of tori (1 and 2, respectively) and in the location where magnetic reconnections can occur (circles of ordinary X-points displaced from the equator on top and bottom of the single torus, and equatorial singular current layer between the two tori, respectively).

The possibility of building a PWN-like reconnection machine in the laboratory is being explored, in anticipation of devising a straightforward modification of PROTO-SPHERA. Obviously two anodes on top and bottom would be required, while a single cathode would be needed on the equator of the machine. However, the main challenge will be to find a way to devise boundary conditions capable of emulating the existence of the rotating Pulsar in the center of the PWN-like reconnection machine.

Data availability statement

All data that support the findings of this study are included within the article (and any supplementary files).

Acknowledgment

Annamaria Pau gratefully acknowledges the funding contribution from National Center on HPC, Big Data and Quantum Computing CN00000013. This manuscript reflects only the authors' views and opinions, neither the European Union nor the European Commission can be considered responsible for them.

Appendix A. Force-free fields models and relaxed states in Astrophysics and in laboratory plasmas

Force-free field configurations (referred to with the acronym *ffmf*) [38, 39] are self-consistent distributions of magnetic field \vec{B} and electric current density \vec{j} such that $\vec{j} \wedge \vec{B} = 0$. Apart from the trivial vacuum case ($\vec{j} = 0$), this usually means $\vec{\nabla} \wedge \vec{B} = \mu \vec{B}$. Magnetic field and current density are therefore aligned inside the plasma with a proportionality parameter $\mu = \mu_0 \vec{j} \cdot \vec{B} / B^2$. *ffmf*s are not subject to Lorentz forces. Hence, their currents and fields can decay exponentially without causing material fluid motions [40], with long e-folding times (compatible with the tiny resistivity of astrophysical plasmas and the smallness of other dissipative effects). These times are much longer than the time scales caused by a direct Lorentz force and the consequent plasma motions. These two reasons make *ffmf*s the simplest choice for describing long-lasting large-scale magnetic structures in Astrophysics and can very often provide an inspiration for magnetic confinement configurations in laboratory plasmas. One could summarize their relevance by stating that: if currents are unavoidable in Astrophysics and in magnetic confinement configurations, let them flow along the field.

In a perfectly conducting plasma (with resistivity $\eta = 0$ and moving with velocity \vec{V} , such that $\vec{E} + \vec{V} \wedge \vec{B} = 0$): $\partial \vec{A} / \partial t = \vec{V} \wedge \vec{B} + \vec{\nabla} \chi$, where χ is an arbitrary gauge [7]. The parallel component of the vector magnetic potential \vec{A} satisfies the magnetic differential equation: $\vec{B} \cdot \vec{\nabla} \chi = \vec{B} \cdot \partial \vec{A} / \partial t$. To make the gauge χ single-valued it is necessary, respectively, that $\oint \frac{d\vec{A}}{B} \cdot \frac{\partial \vec{A}}{\partial t}$ is zero on any field line and furthermore, if the field is not ergodic, that $\oint \frac{d\vec{A}}{|\nabla \psi|} \cdot \frac{\partial \vec{A}}{\partial t}$ is zero upon any magnetic surface, which can be labeled by the poloidal (ψ) or toroidal ($\psi_T(\psi)$) flux enclosed inside it. So, for every flux tube labelled (Klebsch representation) by constant values of the two variables (α, β) , $K(\alpha, \beta) = \int \vec{A} \cdot \vec{B} dV$ is an invariant, called magnetic helicity. The physical meaning of the magnetic helicity for flux tubes has been illustrated in a number of papers [41, 42]. It is a measure of how much the lines of force are interlinked, kinked or twisted and it is a slowly decaying invariant [43]. In the presence of finite resistivity ($\eta \neq 0$), magnetic reconnections redistribute $\vec{A} \cdot \vec{B}$ over the plasma volume [44].

In the case of non-ergodic *ffmf*s (among which axisymmetric confinement configurations of toroidal shape are the most familiar examples), the magnetic fields and the electric currents are flowing on magnetic surfaces. A number of integral quantities are preserved by the magnetic reconnections [45], they can be expressed as: $K_\delta = \int (\chi_{\text{hel}})^\delta (\vec{A} \cdot \vec{B}) dV$, where $\chi_{\text{hel}}(\psi) = q\psi_T - \psi$ is the helical flux of the resonant surface upon which the magnetic reconnection occurs. In this expression the safety factor on a magnetic surface is indicated by $q(\psi)$ (inverse of the rotational transform on the same surface, $q(\psi) = 1/\iota(\psi)$). The Taylor helicity invariant $K = \int \vec{A} \cdot \vec{B} dV$, with $(\chi_{\text{hel}})^0$, is however the only common invariant for all safety factors and so for all resonant surfaces.

The Taylor assumption [7] is that in the plasma the magnetic energy decays to its minimum value, and is subject to the conservation of magnetic helicity K defined for closed field structures (flux tubes), contained within a magnetic surface (where $\vec{B} \cdot \vec{n} = 0$). Minimizing the magnetic energy $W = (1/2\mu_0) \int (\vec{\nabla} \wedge \vec{A})^2 dV$, under the constraint that $K = \text{constant}$, the Beltrami equation is obtained: $\vec{\nabla} \wedge \vec{B} = \mu \vec{B}$; $\vec{B} \cdot \vec{\nabla} \mu = 0$, which describes a force-free magnetic field. This explains why in *ffmf*s the proportionality parameter μ is termed as relaxation parameter.

The parameter μ can therefore be a local function of the flux surface: $\mu = \mu(\psi)$, which takes the name of in-homogeneous or non-linear force-free field. A typical example in the case of a toroidal plasma is a single resonant magnetic island formed by an instability on a flux surface where the rotational transform is a rational number $\iota = n/m$. Inside such an island the plasma pressure gradient becomes null, $\vec{\nabla} p = 0$, and the magnetic field is locally force-free, $\vec{j} \wedge \vec{B} = 0$. In other cases, where the relaxation parameter μ is constant not only on a flux surface but all over the space, *ffmf*s take the name of homogeneous *ffmf*s. A typical example is a toroidal plasma in which many resonant flux surfaces reconnect across the whole cross section, leading to ergodicity of the magnetic field, and to global flattening of the plasma pressure gradient, $\vec{\nabla} p = 0$. Moreover, the whole magnetic field is globally force-free, $\vec{j} \wedge \vec{B} = 0$. Since any two homogeneous *ffmf*s with same μ can be freely summed to produce a different *ffmf*, again with the same value the relaxation parameter μ , homogeneous *ffmf*s are described by linear algebra, and also take also the name of linear *ffmf*s. In order to describe jet + torus plasmas the next appendix B to this paper will start from linear *ffmf*s, which provide the simplest analytical description. The homogeneous and linear *ffmf*s also take also the name of relaxed plasma states.

Appendix B. CKF linear force-free fields with up/down even-symmetry

A linear *ffmf* jet + torus plasma configuration was introduced when the PROTO-SPHERA experiment was being designed, as a simply connected magnetic confinement scheme. It is the superposition of two axisymmetric homogeneous force-free fields, each with the same value of the relaxation parameter $\mu = \mu_0 \vec{j} \cdot \vec{B} / B^2$. The first is the up/down even-symmetric Chandrasekhar–Kendall *ffmf* [9] of order-1, which in spherical geometry (r, ϑ, φ) admits the poloidal flux function: $\psi_{\mu}^{\text{CK,even}}(r, \vartheta) = -(\mu r) j_1(\mu r) \sin \vartheta P_1^1(\cos \vartheta)$, see figure B1(a), where $j_1(\mu r)$ is the order 1 spherical Bessel function, having its m th radial zero at $(\mu r) = x_{1,m}$, and $P_1^1(\cos \vartheta)$ is the Legendre polynomial of order 1. The Chandrasekhar–Kendall *ffmf* is an expedient way of modeling a torus, to the point that it was adopted as the base of the spheromak configurations [46, 47]. The relaxation parameter is chosen here as $\mu = x_{1,4} = 14.066$, so that within a unitary sphere four zeroes of $\psi_{\mu}^{\text{CK,even}}$ are present in the Chandrasekhar–Kendall field. The second is the up/down even-symmetric Furth square-toroid *ffmf* [10], which can be written as: $\psi_{\mu}^{\text{CK,even}}(r, \vartheta) =$

$\sqrt{\mu^2 - \lambda^2} r \sin \vartheta J_1(\sqrt{\mu^2 - \lambda^2} r \sin \vartheta) \cos(\lambda r \cos \vartheta)$, see figure B1(b), for any value of $\lambda < \mu$, where J_1 is the cylindrical Bessel function of order 1. The Furth square-toroid *ffmf* is an expedient to model a central jet. The zero-matching parameter λ of the Furth square toroid field is chosen as: $\lambda = (\pi \bullet x_{1,4}) / (2x_{1,3}) = (14.0661939 \bullet \pi) / (2 \bullet 10.904122) = 2.02631$, so that at $R = 0$, $Z = x_{1,3}/x_{1,4} = 0.775$ the zeroes of $\psi_{\mu\lambda}^{\text{F,even}}$ and of $\psi_{\mu}^{\text{CK,even}}$ coincide. This kind of a “number of zeroes” rule on the zero-matching parameter λ helps in obtaining, in the central region near to the origin ($R = 0$, $Z = 0$), a simply connected and closed magnetic field configuration with a unique sign of the toroidal components j_{φ} and B_{φ} . Choosing odd–even zeroes in increasing sequence: 3rd–4th, 5th–6th, 7th–8th, more and more extended jets are obtained. Using a constant coefficient γ , the superpositions of the two force-free fields are written: $\psi_{\mu\lambda}^{\text{even}}(r, \vartheta) = \psi_{\mu}^{\text{CK,even}} + \gamma \psi_{\mu\lambda}^{\text{F,even}}$, see figures B2(c) and (d). When $\gamma \geq 0.402$, they contain, in a simply connected region near to the origin, a toroidal current density j_{φ} with the same sign (here assumed to be positive) and can be called CKF *ffmf*s [11, 48]. They are simply-connected axisymmetric plasma equilibria, more complex than spheromaks, since they contain a magnetic separatrix ($\psi = \psi_X$) with ordinary X-points ($B_{\text{poloidal}} = 0$, but $B_{\text{toroidal}} \neq 0$) lying on two circles. The separatrix divides a main spherical torus (ST), two secondary tori (SC) on top and bottom of it and a surrounding plasma (SP) that embeds all the three tori, see figure B1(c).

The main ST plasma of figure B1(c) has an MHD safety factor $q_0^{\text{ST}} \approx 1.0$ on the magnetic axis ($\psi = \psi_{\text{axis}}$), and $q_{95}^{\text{ST}} \approx 1.5$ at its edge ($q_{95}^{\text{ST}} = \psi_{\text{axis}} - 0.95 \cdot [\psi_{\text{axis}} - \psi_X]$). The two secondary plasma tori (SCs), on top and bottom of the main torus, also have $q_0^{\text{SC}} \approx 1.0$ on their magnetic axes ($\psi = \psi_{\text{SC}}$) and $q_{95}^{\text{SC}} \approx 1.5$ at their edges ($q_{95}^{\text{SC}} = \psi_{\text{SC}} - 0.95 \cdot [\psi_{\text{SC}} - \psi_X]$). The SP embedding the three tori has a larger safety factor, respectively $q_0^{\text{SP}} \approx 1.5$ on the symmetry axis ($\psi = 0$) and $q_{95}^{\text{SP}} \approx 3.7$ at the separatrix ($q_{95}^{\text{SP}} = 0.95 \cdot \psi_X$). Two degenerate magnetic X-points ($B = 0$) are also present on two single points on the symmetry axis, one at the top and the other at the bottom of the simply connected central configuration.

The value of the constant superposition coefficient γ is less critical than that of the value of the zero-matching parameter λ ; if the superposition coefficient exceeds $\gamma = 0.69$ the SCs disappear. CKF linear (relaxed) force-free fields, with current density \vec{j} aligned everywhere to the magnetic field \vec{B} , with a relaxation parameter $\mu = \mu_0 \vec{j} \cdot \vec{B} / B^2$ constant all over the plasma, cannot sustain any pressure gradient, and the MHD equilibrium requires that $\vec{\nabla} p = 0$.

It should be noted that CKF linear *ffmf*s cannot be realized as localized physical objects, as, beyond the simply connected plasma region near to the origin of the coordinates, other plasma regions with alternating signs of fields and current densities extend to infinity all over the 3D space. The equilibrium of the simply connected plasma region near to the origin is guaranteed only by the presence of this unlimited set of alternating fields and currents.

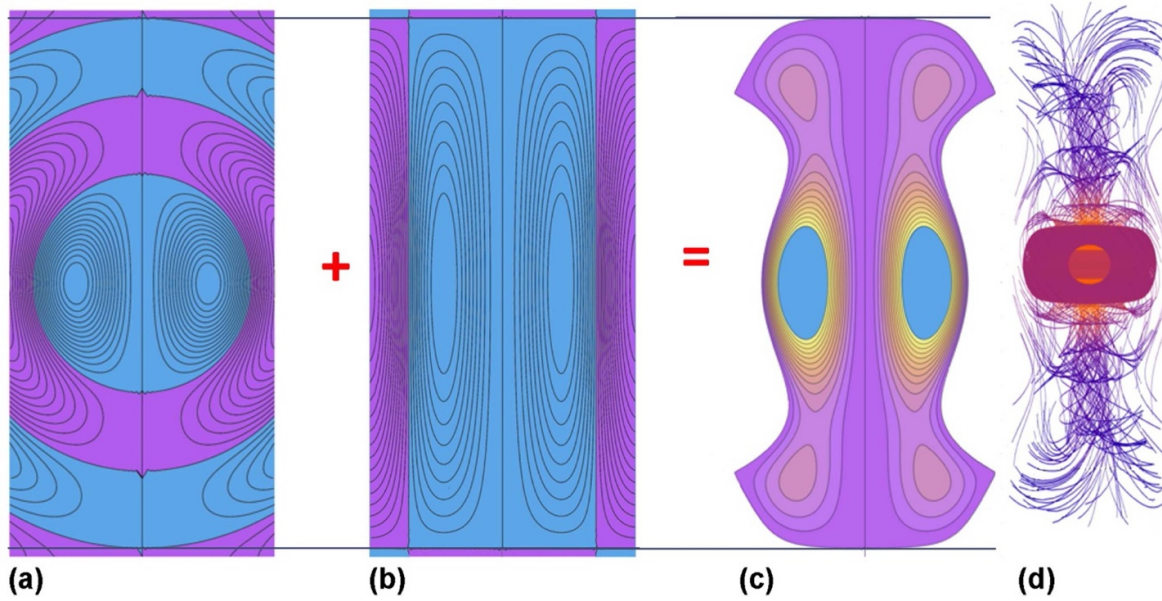


Figure B1. (a) Cross-sections of the axisymmetric Chandrasekhar–Kendall (CK) even-symmetry force-free field $\psi_{\mu}^{\text{CK,even}}$ with relaxation parameter $\mu = x_{1,4} = 14.066$. Geometric scale is chosen such that four zeroes of the CK *ffmf* are contained in a unitary sphere. (b) Cross-sections of the axisymmetric even-symmetry Furth square toroid force-free field (F) $\psi_{\mu\lambda}^{\text{F,even}}$ with same $\mu = 14.066$ and zero-matching parameter $\lambda = (\pi \bullet x_{1,4})/2x_{1,3} = 2.026$ at the third zero of the CK *ffmf*. (c) Cross-sections of the poloidal flux function of axisymmetric even-symmetry CKF force-free field: $\psi_{\mu\lambda}^{\text{even}}(r, \vartheta) = \psi_{\mu}^{\text{CK,even}} + \gamma \psi_{\mu\lambda}^{\text{F,even}}$, with constant superposition coefficient $\gamma = 0.40$, detailing its composition in terms of different plasma regions, divided by a magnetic separatrix. (d) Field-line-tracing of jet + torus linear CKF *ffmf*.

The ideal MHD stability of the CKF force-free fields has been studied by solving the spectral eigenvalue problem [49]: $\overleftrightarrow{W}_n \cdot \vec{\xi}_n = \omega_n^2 \overleftrightarrow{K}_n \cdot \vec{\xi}_n$, for any toroidal mode number n of the perturbation, where the tensor \overleftrightarrow{W}_n is the spectral plasma perturbed potential energy and the tensor \overleftrightarrow{K}_n the spectral plasma perturbed kinetic energy, associated with the perturbed plasma displacement $\vec{\xi}_n$. Whereas in the ideal MHD stability analysis of any axisymmetric equilibrium, the perturbation can be separated on the base of the toroidal mode number n , the poloidal mode numbers m are not-separable in any kind of magnetic coordinates: the perturbed spectral energies become tensors because of the mixing of poloidal mode numbers m . The expressions for the perturbed energies become simpler [50] if the equilibrium is analyzed in non-orthogonal periodical Boozer coordinates (ψ_T -radial = toroidal flux, θ -poloidal, ϕ -toroidal) [51], with Jacobian $\sqrt{g} \propto 1/B^2$. More details on these coordinates can be found in [48]. At the edge of the CKF *ffmf*s (toroidal flux $\psi_T = \psi_T^{\text{max}}$, corresponding to the poloidal flux $\psi = 0$) fixed-boundary conditions have been considered, they mean the plasma radial displacement $\xi_n^{\psi} = \vec{\xi}_n \cdot \vec{\nabla} \psi_T$ is null: $\xi_n^{\psi} = (\psi_T^{\text{max}}) = 0$; the result of the ideal MHD stability calculations for low toroidal mode numbers ($n = 1, 2, 3$) is that the CKF *ffmf*s are stable in fixed-boundary when the value of the constant superposition coefficient is greater than $\gamma = 0.5$, see figure B2, i.e. when the total current inside the jet is large enough, compared to the total current inside the torus. Since CKF linear *ffmf*s cannot be calculated as localized equilibria, their free-boundary ideal MHD stability does not have any significance.

Appendix C. Chandrasekhar-Kendall-Furth un-relaxed equilibrium configurations

CKF homogeneous and in-homogeneous force-free fields have therefore $\nabla p = 0$ and are so unable to confine plasmas of fusion interest, but un-relaxed ($\vec{j} \wedge \vec{B} \neq 0$, $\vec{\nabla} p \neq 0$) CKF equilibria have also been evaluated numerically [11]. The calculations used the boundary condition that the relaxation parameter μ is constant at the edge of the plasma. This is connected with the idea of helicity injection into magnetic configurations of fusion interest, which can be traced back to Taylor [8, 52] as well. The origin of magnetic helicity injection is connected with the electric current forced to flow along a DC magnetic field, which generates perpendicular magnetic flux and causes the magnetic field lines to kink up, with a helical pattern. Then, magnetic flux, plasma current and magnetic energy will be injected along with the helicity. But the question about un-relaxed equilibria is: how does the helicity injected from the boundary $\psi = \psi_{\text{edge}} = 0$ diffuse toward the center of the plasma $\psi = \psi_{\text{axis}}$? A guess can be found calculating the ratio between the variation of magnetic energy and that of magnetic helicity in fully relaxed states, that is $d(\Delta W)/d(\Delta K) = \mu/2\mu_0$. This indicates that the helicity flows from higher to lower μ values. A helicity transfer from a flux tube with larger μ to a flux tube with smaller μ lowers indeed the overall magnetic energy of the two flux tubes. In other words, magnetic reconnection processes will convert part of the magnetic energy into kinetic energy of the magnetized plasma. For un-relaxed CKF equilibria, where μ is no longer constant on every flux surface, the surface-averaged value of the relaxation

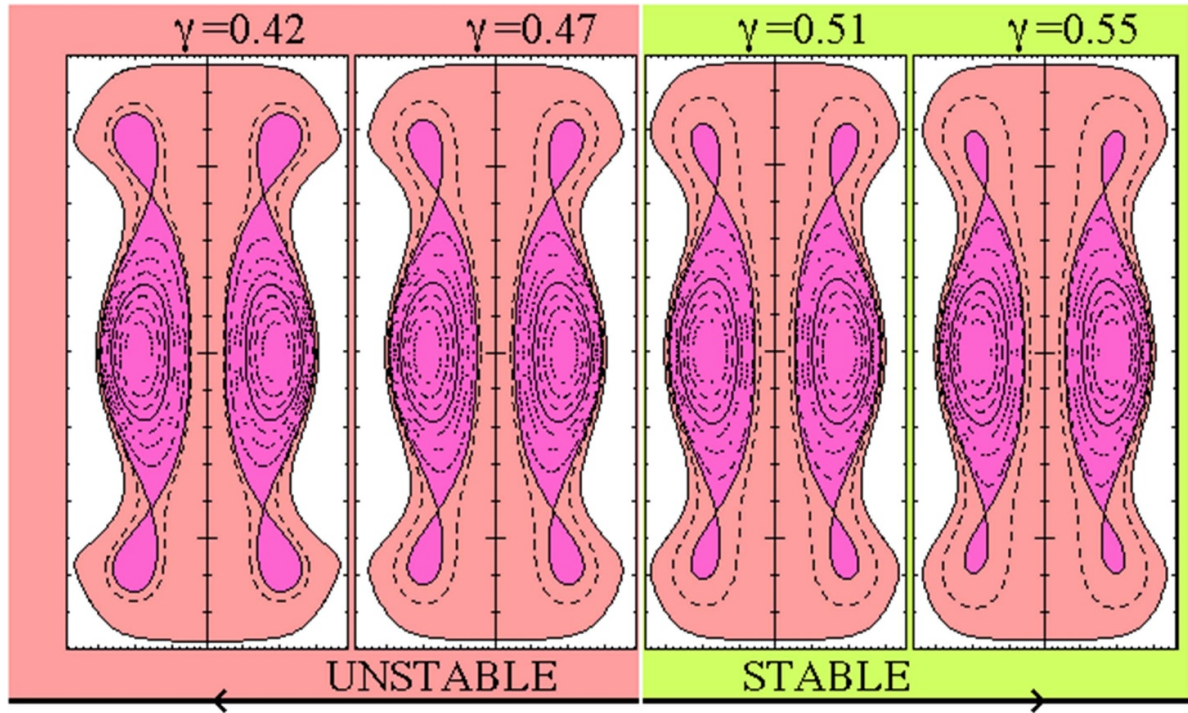


Figure B2. Sequence of cross-sections of CKF even-symmetry force-free fields with ideal MHD stability boundary as a function of the constant superposition coefficient γ . Geometric scale is arbitrary.

parameter $\langle \mu \rangle = \mu_0 \langle \vec{j} \cdot \vec{B} / B^2 \rangle$ is therefore assumed to be decreasing from the edge of the SP to the axis of the main ST.

In CKF un-relaxed equilibria, if the SP could be sustained by driving current on its closed flux surfaces, magnetic helicity would flow down the $\langle \mu \rangle$ gradient and would be injected into the main ST, through magnetic reconnections at the two circles of ordinary X-points, where $\psi = \psi_X$, as shown in figure C1(a). The gradient of the plasma pressure profile $\vec{\nabla} p$ is assumed to be concentrated in the same region where the gradient of the surface averaged relaxation parameter $\vec{\nabla} \langle \mu \rangle$ has the largest variation and to be null where μ is constant. Inside the SP ($0 < \psi < \psi_X$) the relaxation parameter $\mu(\psi)$ is assumed to take the constant value μ_{edge} , until the separatrix ψ_X , while the plasma pressure p remains constant at its edge value p_{edge} . The drop in the relaxation parameter from the edge ($\psi = \psi_{\text{edge}} = 0$) to the axis of the ST plasma ($\psi = \psi_{\text{axis}}$) is $\Delta\mu = \mu_{\text{edge}} - \mu_{\text{axis}}$ and the drop in the plasma pressure Δp from the ST axis to the edge of the ST plasma is $\Delta p = p_{\text{axis}} - p_{\text{edge}}$. The width of both profiles is such that $\vec{\nabla} p$ and $\vec{\nabla} \langle \mu \rangle$ are concentrated in an interval of flux surfaces internal to the circles of ordinary X-points, which can reach at most the ST axis: $\psi_X < \psi < \psi_c \leq \psi_{\text{axis}}$. The pressure p is finally supposed to remain constant at p_{axis} and μ to remain constant at μ_{axis} inside the innermost part of the ST plasma ($\psi_c < \psi \leq \psi_{\text{axis}}$).

A variety of un-relaxed ($\vec{\nabla} \langle \mu \rangle \neq 0$, $\vec{\nabla} p \neq 0$) MHD fixed-boundary equilibria have been calculated by Grad-Shafranov solvers, specifically developed for the design of

PROTO-SPHERA [53, 54], which were validated against other equilibrium solvers.

The un-relaxed CKF equilibria are topologically similar to the homogeneous CKF force-free fields of section 2, but the shapes of their plasma boundaries have been modified. The comparison between figures C1(a) and (b) shows that just filling with pressure the shapes of the homogeneous CKF force-free-fields would lead to an increase of the aspect ratio of the main ST and therefore to an excessive lowering of the MHD safety factor q_{95}^{ST} , which would be detrimental for the MHD stability. Un-relaxed CKF equilibria also contain spherical tori (with safety factor $q_0^{\text{ST}} \sim 1.0$ on axis and $q_{95}^{\text{ST}} \sim 2.0$ at the separatrix), secondary tori (with safety factors $q_0^{\text{SC}} \sim 1.0$) and are embedded into a SP with higher safety factor ($q_0^{\text{SP}} \sim 3$ on the symmetry axis and $q_{95}^{\text{SP}} \sim 5$ at the separatrix). The un-relaxed CKF configurations can be contained in an almost cylindrical solenoid by simply compressing external PF coils; see figure C1(c), calculated from a free-boundary equilibrium solver [11]. The required total current flowing inside all the compressing poloidal field coils is almost equal to the total toroidal current inside the main ST.

Since CKF un-relaxed configurations can be calculated as localized equilibria, the assessment of their ideal free-boundary stability becomes relevant.

Un-relaxed CKF equilibria, with this kind of $\langle \mu \rangle$ and pressure profiles, can be stable in free-boundary conditions ($\xi^{\psi_n}(\psi_T^{\text{max}}) \neq 0$) to all ideal MHD perturbations with low toroidal mode number ($n = 1, 2, 3$) [15], up to order-unity volume-averaged beta values $\langle \beta \rangle_{\text{vol}} = 2\mu_0 \langle p \rangle_{\text{vol}} / \langle B^2 \rangle_{\text{vol}} = 1$.

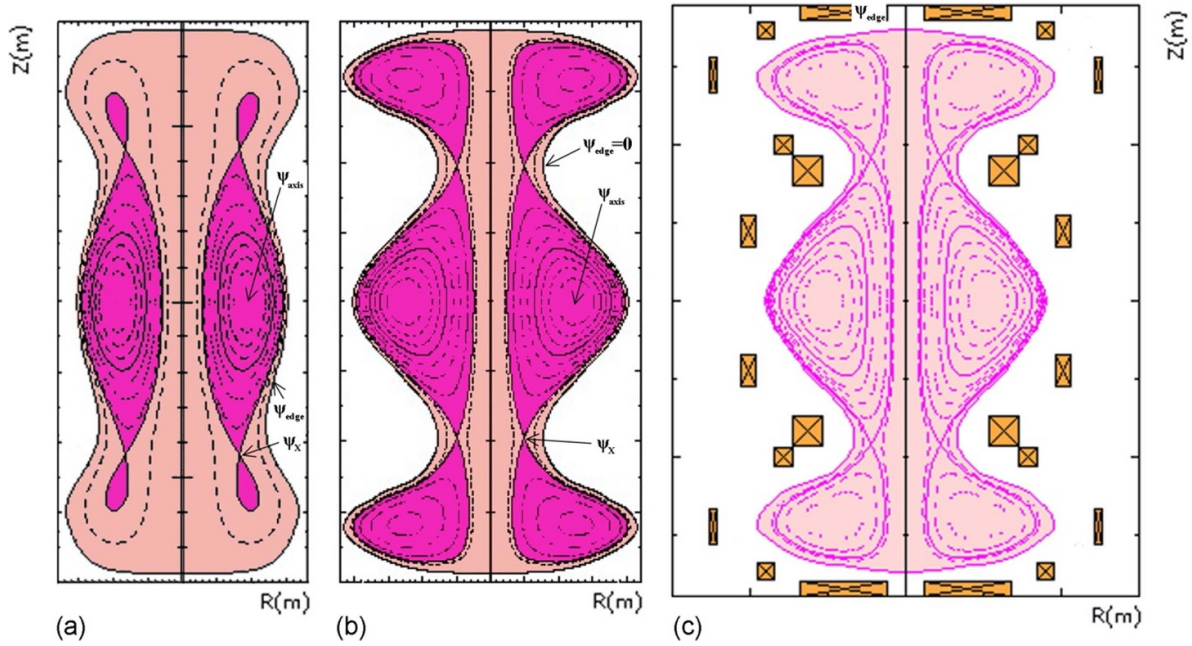


Figure C1. (a) Cross-section of linear *fmf* even-symmetry CKF magnetic configuration with constant superposition coefficient $\gamma = 0.55$. (b) Cross-section of un-relaxed CKF equilibrium with volume averaged beta $\langle \beta \rangle_{vol} = 1.02$. (c) Un-relaxed CKF equilibrium calculated in free-boundary mode, with magnetic compression coils able to contain the plasma. Geometric scale is arbitrary.

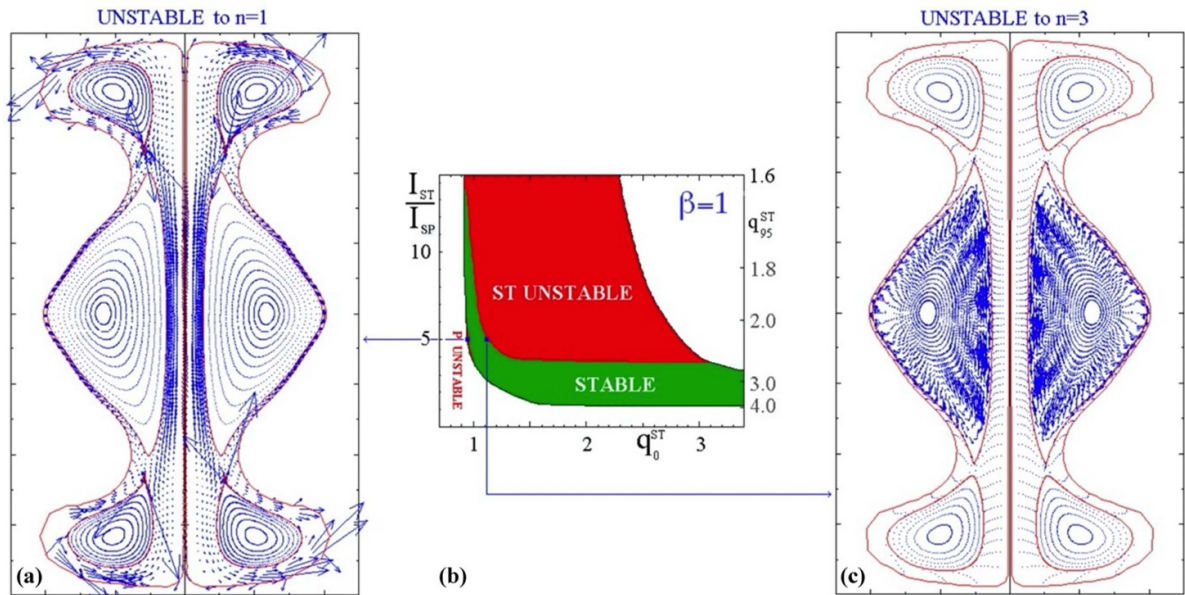


Figure C2. Behaviour of ideal MHD free-boundary stability for un-relaxed CKF configurations at $\beta = 1$. (a) Arrow plot of global SP tilt mode at low q_0^{ST} . (b) Ideal stability boundary as a function of q_0^{ST} and I_{ST}/I_{SP} . (c) Arrow plot of instability of ST at high q_0^{ST} , which is almost a fixed-boundary instability.

This happens provided that the ratio between the total plasma current flowing inside the main ST and the total plasma current flowing inside the SP is less than 4: $I_{ST}/I_{SP} < 4$, see figure C2(b). The modes which limit the stability boundary are a tilt of the SP at low q_0^{ST} , see figure C2(a), and an almost fixed-boundary instability of the ST at high q_0^{ST} , see figure C2(c).

Appendix D. Model for helicity injection in PROTO-SPHERA

In the presence of open field lines, where \vec{B} ends on electrodes, as in the PROTO-SPHERA case, $K = \int \vec{A} \cdot \vec{B} dV$ is no longer invariant to an arbitrary gauge χ . But if an open vacuum field

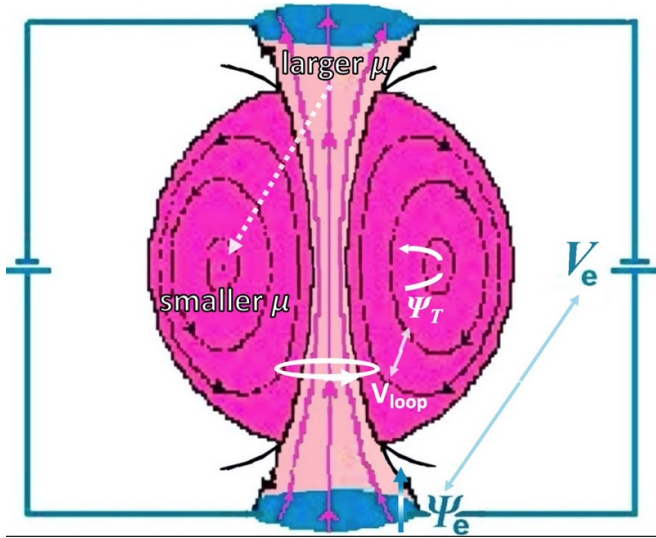


Figure D1. Scheme of helicity injection on an electrode experiment, like PROTO-SPHERA. The DC helicity injection rate is twice the product of the poloidal flux through the electrodes Ψ_e times the DC voltage between electrodes V_e , whereas the AC induction helicity injection would be twice the product of the toroidal flux ψ_T inside the torus times the inductive loop voltage V_{loop} around the torus.

\vec{B}_{vac} , having zero helicity and with the same boundary conditions of \vec{B} on the electrodes is introduced, in this case, a relative magnetic helicity [41] ΔK replaces K and it results: $\Delta K = \int (\vec{A} + \vec{A}_{vac}) \cdot (\vec{B} - \vec{B}_{vac}) dV$. The relative magnetic helicity ΔK is well-defined (with respect to gauge invariance) and enjoys the same properties as K as far as its flow and injection are concerned. In a domain limited by electrodes, the helicity source is the CP with relaxation parameter μ_{CP} and the helicity sink is the ST with relaxation parameter μ_{ST} . A gradient in the relaxation parameter $\vec{\nabla} \langle \mu \rangle = \mu_0 \vec{\nabla} \langle \vec{j} \cdot \vec{B} / B^2 \rangle$ appears with $\mu_{CP} > \mu_{ST}$.

The dynamics of the relative magnetic helicity in a domain (its normal \hat{n} pointing outside), can be expressed, see figure D1, through a ‘‘Poynting’s theorem’’ [55]:

$$d(\Delta K)/dt = -2 \int \Phi_e (\vec{B} \cdot \hat{n}) dS - 2 \int (\vec{A} \wedge \partial \vec{A} / \partial t \cdot \hat{n}) dS - 2 \int (\vec{E} \cdot \vec{B}) dV, \text{ where}$$

$-2 \int \Phi_e (\vec{B} \cdot \hat{n}) dS$ represents the DC helicity injection and Φ_e is the electrostatic potential on the boundary; the injection rate is $|d(\Delta K)/dt| = 2V_e \Psi_e$, where V_e is the voltage applied between the two electrodes and $\Psi_e = \int (\vec{B} \cdot \hat{n}) dS$ is the poloidal magnetic flux which enters or exits from each of the electrodes. Through reconnections at the X-points, flux surfaces enter from the CP into the edge of the torus and are dissipated while they move toward its magnetic axis; other flux surfaces are expelled into the private region of the divertor tails on top and bottom of the torus.

$-2 \int (\vec{A} \wedge \partial \vec{A} / \partial t \cdot \hat{n}) dS$ represents the AC helicity injection and includes the inductive helicity injection (ohmic drive) $|d(\Delta K)/dt| = 2V_{loop} \psi_T$, where V_{loop} is the loop voltage applied by any kind of central transformer and ψ_T is the toroidal flux inside the torus. In ohmic drive flux surfaces generated by the central solenoid enter the torus and are dissipated inside it.

$-2 \int (\vec{E} \cdot \vec{B}) dV$ represents the total helicity dissipation.

DC helicity injection can be considered as a steady-state replacement of transient Ohmic drive.

ORCID iDs

- Franco Alladio <https://orcid.org/0000-0002-1176-3017>
 Paolo Micozzi <https://orcid.org/0009-0002-5411-820X>
 Luca Boncagni <https://orcid.org/0009-0008-7287-4715>
 Annamaria Pau <https://orcid.org/0000-0002-4946-0302>
 Shayesteh Naghinajad <https://orcid.org/0000-0002-6821-131X>
 Samanta Macera <https://orcid.org/0009-0002-7321-3456>
 Paolo Buratti <https://orcid.org/0000-0001-8426-3163>
 Francesco Filippi <https://orcid.org/0000-0002-8983-556X>
 Giuseppe Galatola Teka <https://orcid.org/0000-0002-7595-4568>
 Francesco Giammanco <https://orcid.org/0000-0003-2621-3541>
 Edmondo Giovannozzi <https://orcid.org/0000-0002-0939-5120>
 Matteo Iafrati <https://orcid.org/0000-0003-4649-9065>
 Alessandro Lampasi <https://orcid.org/0000-0003-4395-3496>
 Paolo Marsili <https://orcid.org/0000-0002-5029-5826>

References

- [1] Alladio F, Costa P, Mancuso A, Micozzi P, Papastergiou S and Rogier F 2006 *Nucl. Fusion* **46** S613–24
- [2] Micozzi P et al 2024 *Plasma Sci. Technol.* **26** 005100
- [3] Tavani M et al 2011 *Science* **331** 736–73
- [4] Pucci F et al 2020 *J. Plasma Phys.* **86** 6
- [5] ESA/Hubble credit 2017 *Chandra X-ray Observatory (X-ray) Image of the Crab Nebula* (available at: <https://esahubble.org/images/potw1720f/>)
- [6] Beltrami E 1889 *Int. J. Fusion Energy* **3** 51–57 (available at: www.researchgate.net/file.PostFileLoader.html?id=58920519615e277e342ced8&assetKey=AS%3A456982680346624%401485964569318)
- [7] Taylor J B 1986 *Rev. Mod. Phys.* **58** 741
- [8] Taylor J B 1974 *Phys. Rev. Lett.* **33** 1139
- [9] Chandrasekhar S and Kendall P C 1957 *Astrophys. J.* **41** 457
- [10] Furth H P, Levine M A and Waniek R W 1957 *Rev. Sci. Instrum.* **28** 949
- [11] Rogier F, Bracco G, Mancuso A, Micozzi P and Alladio F 2003 Simply connected high- β magnetic configurations *11th Int. Congress on Plasma Physics: ICPP 2002 (Sidney, Australia, 15–19 July 2002)* (American Institute of Physics) vol 669 p 557 (available at: www.researchgate.net/publication/234851157_Simply_Connected_High-b_Magnetic_Configurations)
- [12] Alladio F et al 2001 ENEA Serie Energia Associazione Euratom-ENEA sulla Fusione RT/ERG/FUS/2001/14 (available at: www.afs.enea.it/project/protosphaera/webdocs/docs/Full_PROTO-SPHERA_Report_2001.pdf)
- [13] Alladio F et al 2000 Results of proto-pinch testbench for the PROTO-SPHERA experiment *Proc. 27th EPS Conf. on Contr. Fusion and Plasma Phys (Budapest, 12–16 June 2000)* vol 24B pp 161–4 (available at: www.researchgate.net/publication/242323182_Results_of_Proto-Pinch_Testbench_for_the_Proto-Sphaera_experiment)

- [14] Micozzi P, Alladio F, Mancuso A and Rogier F 2010 *Nucl. Fusion* **50** 095004
- [15] Alladio F, Mancuso A, Micozzi P and Rogier F 2007 *Phys. Plasmas* **14** 082508
- [16] Sykes A et al 1992 *Nucl. Fusion* **32** 694
- [17] Cormack A M 1963 *J. Appl. Phys.* **34** 2722–7
- [18] Zernike F 1934 *Physica* **1** 689–704
- [19] Damizia Y, Iafrazi M, Liuzza D, Boncagni L, Micozzi P and Alladio F 2021 *Fusion Eng. Des.* **169** 112461
- [20] Natterer F 2013 *The Mathematics of Computerized Tomography* (Springer) (available at: <https://link.springer.com/book/10.1007/978-3-663-01409-6>)
- [21] Kak A C and Slaney M 1993 *Principles of Computerized Tomographic Imaging* (IEEE Press) (available at: www.slaney.org/pct/pct-toc.html)
- [22] Kazantsev S G 2015 *J. Inverse Ill-Posed Probl.* **23** 173–85
- [23] Naghinajad S and Pau A 2023 *3D Ultrasonic Tomography for Image Reconstruction: An Application to the Plasma Dynamics of PROTOSPHERA VII ECCOMAS Young Investigators Conf. YIC2023 (Porto, Portugal, 19–21 June 2023)* (available at: <https://zenodo.org/records/8393048>)
- [24] García-Martínez P L, Lampugnani L G and Farengo R 2014 *Phys. Plasmas* **21** 122511
- [25] Goldreich P and Julian W H 1969 *Astrophys. J.* **157** 869–80
- [26] Michel F C 1991 *Theory of Neutron Star Magnetospheres* (University of Chicago Press) (available at: <https://press.uchicago.edu/ucp/books/book/chicago/T/bo3641575.html>)
- [27] NASA, ESA, J. DePasquale (STScI), and R. Hurt (Caltech/IPAC) 2020 *Crab Nebula* (available at: <https://hubblesite.org/contents/media/images/2020/03/4601-Image>)
- [28] Kumar D, Bhattacharyya R and Smolarkiewicz P K 2013 *Phys. Plasmas* **20** 112903
- [29] Reich W 2002 Radio observations of supernova remnants *Proc. 270. WE-Heraeus Seminar on Neutron Stars, Pulsars, and Supernova Remnants* e-Print: astro-ph/0208498 [astro-ph]
- [30] Bucciantini N et al 2023 *Nat. Astron.* **7** 602–10
- [31] Tananbaum H, Weisskopf M C, Tucker W, Wilkes B and Edmonds P 2014 *Rep. Prog. Phys.* **77** 066902
- [32] Ng C-Y and Romani R W 2004 *Astrophys. J.* **601** 479–84
- [33] Xie F et al 2022 *Nature* **612** 658–60
- [34] Cerutti B and Giacinti G 2021 *Astron. Astrophys.* **656** A91
- [35] Schaller E L and Fesen R A 2002 *Astron. J.* **123** 941
- [36] Hester J J, Mori K, Burrows D, Gallagher J S, Graham J R, Halverson M, Kader A, Michel F C and Scowen P 2002 *Astrophys. J.* **577** L49
- [37] Uzdensky D A and Spitkovsky A 2014 *Astrophys. J.* **780** 3
- [38] Chandrasekhar S and Woltjer L 1958 *Proc. Natl Acad. Sci.* **44** 4
- [39] Marsh G E 1998 *Force-Free Magnetic Fields: Solutions, Topology and Applications* (World Scientific) (available at: www.worldscientific.com/worldscibooks/10.1142/2965#t=aboutBook)
- [40] Lundquist S 1950 *Arkiv Fysik* **2** 35
- [41] Berger M A and Field G B 1984 *J. Fluid Mech.* **147** 133
- [42] Pfister H and Gekelman W 1991 *Am. J. Phys.* **59** 497
- [43] Moffat H K 2015 *J. Plasma Phys.* **81** 905810608
- [44] Woltjer R L 1958 *Proc. Natl Acad. Sci. USA* **44** 489–91
- [45] Bhattacharjee A and Dewar R L 1982 *Phys. Fluids* **25** 887
- [46] Rosenbluth M N and Bussac M 1979 *Nucl. Fusion* **19** 489
- [47] Comparison of compact toroid configurations 2000 *Second Research Coordination Meeting (RCM) on Comparison of Compact Toroid Configuration* (International Atomic Energy Agency) (Vienna, Austria, 10–14 July 2000) eds P Bellan and J Dolan (available at: https://vant.kipt.kharkov.ua/ARTICLE/VANT_2000_3/article_2000_3_81.pdf)
- [48] Alladio F, Mancuso A, Micozzi P and Rogier F 2005 *Phys. Plasmas* **12** 112502
- [49] Chance M S, Greene J M, Grimm R C, Johnson J L, Manickam J, Kerner W, Berger D, Bernard L C, Gruber R and Troyon F 1978 *J. Comput. Phys.* **28** 1
- [50] Cooper W A 1992 *Plasma Phys. Control. Fusion* **34** 1011
- [51] Chen F 2011 *An Indispensable Truth: How Fusion Power Can Save the Planet* (Springer) pp 413–4 (available at: <https://link.springer.com/content/pdf/10.1007/978-1-4419-7820-2.pdf>)
- [52] Taylor J B and Turner M F 1989 *Nucl. Fusion* **29** 219
- [53] Alladio F and Micozzi P 1997 *Nucl. Fusion* **37** 1759
- [54] Rogier F and Mancuso A 2004 *Int. J. Comput. Eng. Sci.* **05** 91–112
- [55] Boozer A 1986 *Phys. Fluids* **29** 4123